MASTER

A 6.65 m Normal Incidence Spectrometer (NIS) for high resolution spectroscopy in the VUV

Breuls, M.G.N.

Award date:
1995

FOM-INSTITUUT
VOOR
PLASMAFYSICA
RIJNHUIZEN

ASSOCIATIE
EURATOM-FOM

IR 95/001
June 95

A 6.65 m Normal Incidence Spectrometer (NIS) for high resolution spectroscopy in the VUV

M.G.N. Breuls

A 6.65 m Normal Incidence Spectrometer (NIS) for high resolution spectroscopy in the VUV
by M.G.N. Breuls
June 1995
FOM Report IR 95/001

The work described in this report has been performed to obtain my degree in physics at the Eindhoven University of Technology, Eindhoven, The Netherlands. The research has been carried out at the FOM Institute for Plasma Physics "Rijnhuizen", Nieuwegein, The Netherlands, under the supervision of Prof. Dr. N.J. Lopes Cardozo and Dr. F.G. Meijer.

This work was performed as part of the research programme of the association agreement of Euratom and the "Stichting voor Fundamenteel Onderzoek der Materie" (FOM) with financial support from the "Nederlandse Organisatie voor Wetenschappelijk Onderzoek" (NWO) and Euratom.

Summary

A 6.65 m Normal Incidence Spectrometer (NIS)
for high resolution spectroscopy in the VUV

The FOM Institute contributes to the Euratom research programme to use controlled nuclear fusion to meet the future world energy requirements. A medium sized tokamak at the institute produces thermonuclear plasmas ($T \sim 1$ keV, $n_e \sim 10^{20}$ m^{-3}). The apparatus is well equipped with diagnostic devices to measure a large number of plasma parameters. However the behaviour of impurities and plasma rotations could not be explored yet. To meet this lack of information, a 6.65 m Normal Incidence Spectrometer (NIS) has been moved from the Amsterdam University. It is equipped with two interchangeable gratings. The accessible wavelength region is 35 - 400 nm. The dimensions of the NIS and its grating properties make a spectral resolving power up to 400,000 possible.

At the FOM Institute, the instrument has been successfully adapted to make it suitable for measuring the RTP plasmas. We equipped it with a scanning mirror system, which allows us to measure the spectrum emitted by a well-defined part of the plasma, with a spatial resolution of about 1 cm. We implemented a CCD camera to do high temporal resolved (0.2 ms) measurements. To interpret the data, we developed a highly sophisticated set of programs. A graphical user interface provides fast and easy adjustment of the computer controlled optical system from any terminal. The vacuum system of the NIS is improved by a new control system.

The NIS will be used to measure impurity distributions, ion temperatures, plasma rotations and magnetic fields. A theoretical foundation including a transport-corona model is given. The combination with the RIS (gRazing Incidence Spectrometer, 3 - 40 nm), which will become operational later this year, allows simultaneous measurement of poloidal and toroidal rotations at the same location. We used neon and argon spectra for calibration.

Samenvatting

Een 6.65 m Normale Inval Spectrometer (NIS)
voor hoge-resolutie spectroscopie in het VUV

Het FOM Instituut voor Plasmafysica Rijnhuizen draagt bij aan het onderzoeksprogramma van Euratom naar kernfusie als (toekomstige) energiebron. Het instituut beschikt over een tokamak waarmee thermonucleaire plasmas worden opgewekt ($T \sim 1$ keV, $n_e \sim 10^{20}$ m^{-3}). Deze is uitgerust met vele diagnostieken waarmee een groot aantal plasma parameters tegelijkertijd gemeten kunnen worden. Het gedrag van onzuiverheden in het plasma en plasma rotaties konden echter nog niet onderzocht worden. Om aan dit probleem tegenmoet te komen, werd de met twee verwisselbare tralies uitgeruste 6.65 m Normale Inval Spectrometer (NIS) overgenomen van de Universiteit van Amsterdam. Het waar te nemen golflengte gebied is 35 - 400 nm. Een spectraal oplossend vermogen tot 400.000 is mogelijk, mede dankzij de afmetingen van de NIS en de eigenschappen van de tralies.

Op het FOM Instituut zijn diverse wijzigingen en uitbreidingen aangebracht om de spectrometer optimaal te kunnen inzetten voor het meten aan RTP plasmas. Dankzij het scanning mirror system kan het spectrum worden gemeten dat locaal in het plasma uitgezonden wordt, met een plaatsresolutie van ca. 1 cm. Door middel van een CCD camera kunnen we tijdopgelost meten (0.2 ms). De speciaal ontwikkelde software maakt een efficiënte interpretatie van de data mogelijk. Het eveneens geautomatiseerde optische systeem kan snel een eenvoudig bediend worden dankzij een grafische user interface. Het vacuumsysteem van de NIS werd uitgerust met een nieuw, intelligent controle systeem.

De NIS zal gebruikt worden om ionenconcentraties (onzuiverheden in het plasma), ionentemperaturen, plasmarotaties en magnetische veldsterktes te meten, zoals in de theoretische beschouwing nader wordt toegelicht. De combinatie met de RIS (Rakelingse Inval Spectrometer, 3 - 40 nm), die in de loop van 1995 in gebruik zal worden genomen, zal gelijktijdige meting van toroidale en poloidale plasmarotaties op dezelfde plaats mogelijk maken. Voor het testen en calibreren zijn neon en argon spectra gebruikt.

Contents

Chapter 1

Introduction

1.1 Nuclear fusion and tokamaks

For the coming decades an increasing demand for energy is expected. The limited availability of fossil fuels and the impact on the environment caused by the burning of these fuels, makes the search for alternative energy resources necessary. The renewable energy resources in the world like solar wind and hydro-electric power are enormous, but their usefulness for large-scale energy production is still rather limited. Nuclear fission of heavy nuclei has its radioactive waste and safety problems. Moreover, the fissile fraction of uranium, ^{235}U, will last only for a few decades. However with the introduction of breeder reactors, which use ^{238}U and ^{233}Th as nuclear fuel, the expected energy requirements of the world would be met for several centuries. But the most promising future energy production method is based on controlled thermonuclear fusion. Nuclear fusion is the energy-producing process that continuously takes place in the sun and other stars. In a nuclear fusion reaction two light nuclei react to form a heavier nucleus. The mass deficit between the reaction products and the fuel nuclei is released as energy, which can be converted into electricity.

The fusion reaction most suitable for use in a fusion reactor is the one involving a deuterium (D, the isotope of hydrogen with mass M = 2) and a tritium (T, the isotope of hydrogen with mass M = 3) nucleus:

$$ {}^{2}_{1}D + {}^{3}_{1}T \rightarrow ({}^{4}_{2}He + 3.52\ MeV) + ({}^{1}_{0}n + 14.1\ MeV). \qquad (1.1) $$

This reaction has, compared with other fusion reactions, the highest probability at the lowest threshold energy. Furthermore, it produces the largest amount of (kinetic) energy. Deuterium occurs in all water with an abundance of 0.015%. Tritium is radioactive with a half-life of 12.36 years and does not occur on earth. It has to be made artificially out of lithium, using the neutrons produced in the fusion reaction (1.1):

$$ {}^{6}_{3}Li + {}^{1}_{0}n \rightarrow ({}^{4}_{2}He + 2.05\ MeV) + ({}^{3}_{1}T + 2.73\ MeV). \qquad (1.2) $$

The breeding of tritium produces even an additional amount of energy. The ^{6}Li isotope occurs in large amounts in ore deposits and dissolved in sea water, so the fuel resources on earth for nuclear fusion are almost inexhaustible.

Since the nuclei in (1.1) both have a positive charge, the repelling Coulomb force prevents their reaction. To overcome this force, the nuclei need to have sufficiently high kinetic energy, which corresponds to a temperature T of about 100 million Kelvin (~ 10 keV). At this temperature the deuterium-tritium gas has changed its state from gas to plasma. A plasma is a quasi-neutral gas in which (part of) the electrons have been separated from their atomic nuclei. Thus in a plasma charged particles are present, besides neutral atoms. This greatly influences the behaviour of the plasma and allows for example the use of magnetic fields for confinement. Furthermore the density of nuclei n and the so called energy confinement time τ_E should be large enough for a fusion reactor in order to obtain a sufficiently high reaction rate. The three conditions for a fusion reactor are combined in the Lawson criterion:

$$n \cdot \tau_E \cdot T \geq 4 \cdot 10^{21} \quad [keVsm^{-3}] \quad (\sim 5 \cdot 10^{25} \quad [Ksm^{-3}]) . \tag{1.3}$$

We often use this triple product $n \cdot \tau_E \cdot T$ to indicate how far a fusion device is from a burning plasma. That means, the produced energy by fusion reactions equals the energy losses by emission of particles and radiation.

Tokamak

Because of the required high temperature, a fusion plasma may not touch any material wall. One way to achieve this, is confinement by magnetic fields. The most promising configuration was introduced in 1951 by the Soviet physicists Andrei Sakharov and Igor Tamm. In this so called tokamak-configuration, the plasma is confined to the centre of a toroidal-shaped vessel. The word "tokamak" is derived from the Russian words for "toroidal magnetic chamber". Figure 1.1 explains the principle of a tokamak. A transformer core surrounds a toroidal vacuum vessel (not drawn in the figure). A current in the primary circuit induces a current in the plasma that acts as secondary circuit. This plasma current in turn causes the heating of the plasma by ohmic dissipation and produces a magnetic field in the poloidal direction B_θ. Due to the toroidal geometry, this toroidal field has a $1/R$ dependence, where R is the distance to the axis of the torus. Therefore we often call the inner and outer side of the torus respectively high-field and low-field side. The coils wound around the torus produce a toroidal magnetic field B_ϕ, which combined with the poloidal field gives a helical field. In the ideal situation the particles in the plasma are bound to gyrate around the magnetic field lines. In this way we achieve the confinement of the plasma. The field lines with the same helicity are lying on nested surfaces of constant magnetic field strength, called magnetic or flux surfaces. Because the particles can move freely along the field lines, the temperature and density are constant on a flux surface.

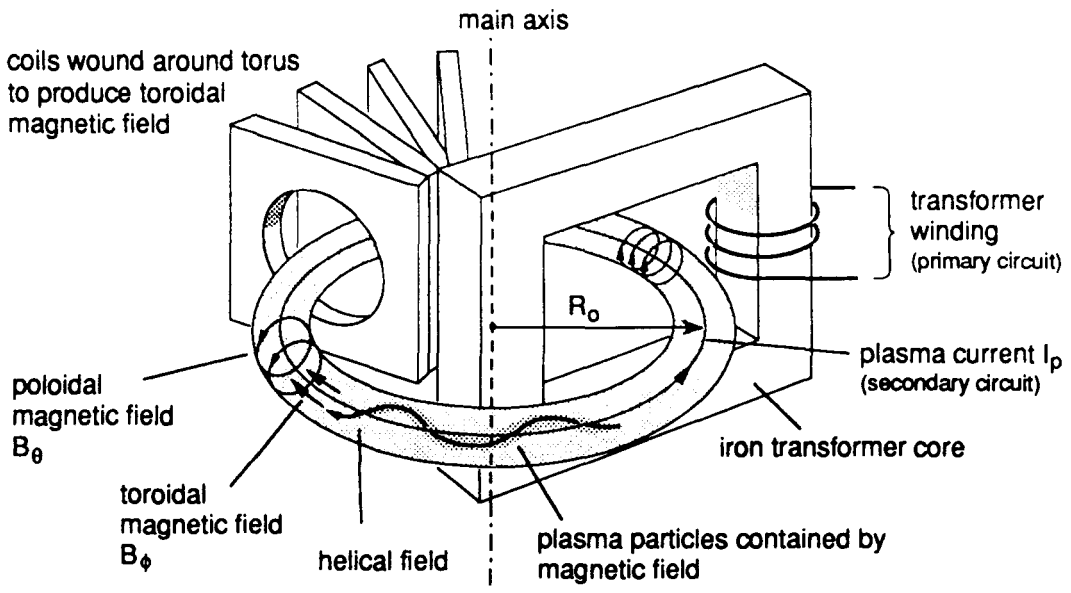

Figure 1.1 - The principle of a tokamak.

Additional heating and self heating

At higher temperatures, the resistance of the plasma becomes too low to allow for effective heating of the plasma by ohmic dissipation. Therefore, for further heating of the plasma, additional methods are necessary. One way to achieve this is Neutral Beam Injection Heating. A beam of charged hydrogen, deuterium or helium is accelerated and, after being neutralised by charge exchange by passing through the parent gas, injected into the plasma. There, the particles transfer their kinetic energy into heat. Local heating of the electrons can be done by means of Electron Cyclotron Resonance Heating (ECRH). The inserted microwave power (60 - 110 GHz) is absorbed at places where the frequency is in resonance with the electron cyclotron frequency, i.e. the gyration frequency of the electrons around the magnetic field lines. Local heating is possible because the electron cyclotron frequency is proportional to the local magnetic field strength, which has a $1/R$ dependence. In the same way local heating of the ions is possible at the much lower ion cyclotron frequencies (due to their larger mass) by injecting radio-frequency power (25 - 55 MHz).

In a future reactor the plasma will have to sustain fusion by self heating due to the kinetic energy released at the reactions. Only the energy carried by the charged reaction products, the ^{4}He-particles, is available for self heating of the plasma. The neutrons escape

from the magnetic fields that confine the plasma. A moderating blanket transfers their energy (80% of the total energy released) into heat. This heat will be used to drive turbines to produce electricity in the conventional way.

Blanket

The blanket surrounding the reactor vessel has several functions. It will most likely consist of a molten F-Li-Be salt and have a thickness of about one meter. Its mean function is to moderate the neutrons. Slowing down collisions are most effective when using light nuclei like Lithium and beryllium. We cannot use hydrogen because this has a too high probability for absorbing the neutrons. This would give energy losses. The lithium in the blanket also provides breeding of tritium by reaction (1.2). The beryllium compensates the neutron losses by diffusion and competing nuclear reactions, by the following neutron-doubling reaction:

$$ {}^{9}_{4}Be + {}^{1}_{0}n \rightarrow 2\,{}^{4}_{2}He + 2\,{}^{1}_{0}n\,. \qquad (1.4) $$

The addition of lost neutrons is necessary since there is only one neutron produced in fusion reaction (1.1), and one tritium nucleus has to be put back into the plasma as new fuel. The addition of fluor has a technical reason: the salt is less corrosive than a mixture of the pure metals. Neutron induced reactions in fluor have low probabilities, so the addition has no side effects.

Safety

The cross-sections of the fusion reactions as a function of temperature have certain maxima. This determines the high plasma temperature needed in a fusion reactor. A favourable implication however is, that if any malfunction increases or decreases the plasma temperature, the reactor will shut down in a short time. The total amount of thermal energy stored in the plasma is less than 1 GJ. This means that the explosive power of a fusion reactor in case of a large-scale accident is even less than that of conventional power stations.
There is no radioactive waste produced in the fusion reactions themselves, but tritium is a radioactive isotope that should be handled with great care. Further there is a very high neutron flux that is not only dangerous itself, but also causes induced radioactivity in the construction materials. Adequate shielding is very important to protect the environment and the apparatus itself against in particular the neutron radiation. The induced radioactivity should be minimised by using (new) construction materials with short induced half-lives, like titanium-vanadium steel.

Advantages and disadvantages of nuclear fusion

The main advantages of nuclear fusion are the almost limitless fuel resources, its inherent safety and its relatively small radioactive waste problems. It also causes no atmospheric pollution leading to a greenhouse effect or acid rain. But there are still many technical and plasma physical problems that have to be solved before a commercial fusion reactor will become available. After a new, larger experimental device, at least one demonstration reactor has to be build. Finally, there are the economical and political problems of nuclear fusion: the investment costs are large and the acceptance of nuclear fusion is hard to predict.

1.2 The Rijnhuizen Tokamak Project (RTP)

One of the main plasma physical problems of nuclear fusion is that the electron energy losses are anomalous. They are about two orders of magnitude larger than predicted by theories based on simple Coulomb particle collisions. These neo-classical theories predict that ion thermal conduction will dominate the energy losses. A possible explanation is the presence of micro-instabilities in the magnetic flux surfaces. Further, experiments showed that the energy confinement time τ_E increases with the electron density n_e, while theory predicted a $1/n_e$ relation. A consequence of these anomalous heat losses is that we need larger, more expensive devices to meet the Lawson criterion (1.3). Another problem is the occurrence of instabilities like disruptions. Disruptions lead to a rapid plasma energy loss and therefore to the end of a discharge. They can occur when the plasma density exceeds a critical value. Finally, the plasma shows rotations in toroidal direction. Rotations in poloidal direction have also been reported.

The RTP tokamak

It is thus clear that transport processes in tokamak plasmas need further research. This is the main research topic of the Rijnhuizen Tokamak Project (RTP) at the FOM (Stichting voor Fundamenteel Onderzoek der Materie) Instituut Rijnhuizen. The Rijnhuizen Tokamak is a medium-sized tokamak, especially designed to analyse plasma properties under different conditions. It is equipped with ECRH systems and a pellet injector to inject small pellets of hydrogen ice into the plasma, so both temperature and density perturbations can be studied. The plasma density varies from $2 \cdot 10^{18}$ to $1.2 \cdot 10^{20}$ m^{-3} and the central electron temperature ranges from 0.4 up to 4 keV. Table 1.1 gives some main machine parameters of RTP.

Table 1.1 - Some main machine and plasma parameters of RTP

Major radius	R_0	*0.72*	*m*
Minor radius at limiter	a	*0.16 - 0.185*	*m*
Plasma volume		*0.39*	m^3
Plasma current	I_p	≤ 250	*kA*
Loop voltage	V_{loop}	≤ 2.5	*V*
Toroidal field	B_ϕ	≤ 2.6	*T*
Flux swing		*1*	*Vs*
Pulse time		*500*	*ms*
ECRH 60 GHz		2×180	*kW*
ECRH 110 GHz		*500*	*kW*
Central electron density	$n_e(0)$	$\leq 2 \cdot 10^{20}$	m^{-3}
Central electron temperature	$\hat{T}_e(0)$	*0.4 - 4.0*	*keV*
Central ion temperature	$\hat{T}_i(0)$	*0.2 - 0.8*	*kev*
Effective atomic mass	Z_{eff}	*1.5*	
Energy confinement time	τ_E	*3 - 10*	*ms*

The RTP tokamak was already well equipped with diagnostic devices, which can be classified into five groups, according to the techniques used: 1) magnetic field and electrical diagnostics, mainly used to control and reproduce the discharges; 2) laser diagnostics like Thomson scattering; 3) microwave diagnostics, for example electron cyclotron techniques and transmission and reflection diagnostics; 4) particle diagnostics and 5) visible light and X-ray tomography. Together, these diagnostics give the possibility to measure a large number of plasma parameters, with high temporal and/or two-dimensional spatial resolution. Some measured quantities are electron density and temperature, emission of radiation, magnetic properties, MHD (magneto hydrodynamic) activity and supra thermal electron distributions. A more detailed description of all diagnostics can be found in [*Donn-91*].

But in spite of the large number of diagnostics, there are still some plasma parameters that could not be explored until recently, e.g. the behaviour of impurities in the plasma and the plasma rotations mentioned before. In order to meet this lack of information, the RTP spectroscopy programme is developed.

1.3 Spectroscopy at RTP

This thesis will cover the RTP spectroscopy programme, especially in the VUV (Vacuum Ultra Violet) region. We can use spectroscopy to measure the following quantities: impurities (species, concentrations, velocities), electron temperature and density (using spectral line intensity ratios), ion densities and influx of particles (using absolute spectral line intensities), plasma rotations (using Doppler wavelength shift), ion temperatures (using Doppler line broadening) and the magnetic field strength (using the Zeeman effect). As can be seen from this list, spectroscopy can be a very powerful diagnostic tool for tokamak plasmas.

The RTP spectrometers

The RTP spectroscopic instrumentation will consist of a VIsible light Spectrometer (VIS), a Normal Incidence vacuum Spectrometer (NIS), a gRazing Incidence Spectrometer (RIS) and a MultiLayer Mirror (MLM) system. These four spectrometers complement each other as concerning both wavelength region and measured parameters.
The visible light spectrometer is a one meter Jarrell-Ash grating spectrometer, covering the wavelength range from 400 to 900 nm. The light from the tokamak plasma is coupled into the spectrometer using three quartz fibres. In this way three adjustable lines of sight into the plasma are available. The VIS is used to measure the edge plasma.
The 6.65 meter normal incidence vacuum spectrometer, the mean subject of this thesis, covers the wavelength range 35 - 400 nm. It is equipped with two interchangeable gratings, and has a resolving power up to 400,000. A scanning mirror system allows two-dimensional scanning of the source point through the plasma. The NIS will be used for high resolution spectroscopy on both core and edge plasma.
The wavelength range from 3 to 40 nm is covered by the grazing incidence vacuum spectrometer. Because of the poor reflectivity at normal incidence of all materials at these low wavelengths, the grazing incidence spectrometer uses the fact that for very large angles of incidence, the reflectivity approaches unity for all wavelengths. The NIS/RIS combination will allow simultaneous measurement of poloidal and toroidal plasma rotations at the same location.
Finally, the five-channel multilayer mirror system covers the soft X-ray wavelength region. It uses mirrors consisting of alternating Fe/C, W/Si or Cr/C layers. These mirrors can reach reflectivities up to 60 per cent at wavelengths down to a few nm. The five channels each have a different viewing position and adjustable central wavelengths. Table 1.2 gives a survey of some main parameters of the RTP spectrometers.

Table 1.2 - Some main parameters of the RTP spectrometers

Spectrometer (type)	*Focal length [mm]*	*Grating [lines per mm]*	*Blaze wavelength [nm]*	*Wavelength range [nm]*	*Resolving power*
VIS (Czerny Turner)	*1000*	*3600*	*500*	*400 - 900*	*50,000 - 200,000*
NIS (Rowland)	*6650*	*1200*	*170*	*110 - 400*	*100,000 - 250,000*
	6650	*2400*	*70*	*35 - 200*	*100,000 - 400,000*
RIS (Rowland)	*6600*	*1800*	*10*	*3 - 40*	*40,000 - 100,000*
MLM	*~ 100*	-	-	*1 - 40*	*< 40*

Chapter 2

Plasma spectroscopy with the NIS

Plasma spectroscopy is inextricably bound up with impurities. They appear to influence both continuum and line radiation to a large extend. What kind of impuries can we expect in a tokamak plasma and how do they get there? Subparagraph 2.1.1 tries to answer these and other questions. In subparagraph 2.1.2 we will derive a transport-corona model. It will be used to model the plasma behaviour and find relations between several plasma parameters.
The NIS uses concave spherical gratings as both diffracting and focussing element. In the second paragraph we will contemplate the properties of these gratings. We will also consider the resolving power of an optical system like the NIS.
Finally, paragraph 2.3 gives an overview of all plasma parameters that can be derived from spectroscopic measurements using the model of §2.1.2. The numerical examples give an indication of the diagnostic power of the NIS.

2.1 Emission by tokamak plasmas

2.1.1 Impurities

Bremsstrahlung

The ionisation level of the hydrogen isotopes is about 13.6 eV, so in a tokamak plasma with typical temperatures of 1 - 10 keV, all hydrogen atoms are ionised. This means that in a pure hydrogen plasma, line radiation plays no role of importance. Only at the outside of the plasma the temperature can be low enough to emit hydrogen Balmer lines in the visible area and Lyman lines in the VUV region. Radiation losses - mainly in the X-ray region - are dominated by so-called bremsstrahlung. It is emitted when an electron is slowed down in the electric field of another charged particle. This free-free radiation gives a continuous spectrum. The total bremsstrahlung power emitted by a hydrogen tokamak plasma having an electron temperature $\hat{T}_e$ [keV] and density $n_e = n_i = n$ [m^{-3}] is approximately [*Wess-87*]:

$$P_{Br(DT)} \approx 5.35 \cdot 10^{-37}\, n^2\, \hat{T}_e^{1/2} \quad [Wm^{-3}] \ . \tag{2.1}$$

Now consider a plasma not only consisting of hydrogen isotopes, but also of impurity elements I with charge Z_I and fractions

$$f_I = n_I / n_i . \tag{2.2}$$

In this formula is n_I the ion density of element I and n_i the hydrogen ion density. Supposing that all atoms are ionised, the total electron density is

$$n_e = n_i + \sum_I n_I Z_I . \tag{2.3}$$

We now find for the Bremsstrahlung power emitted:

$$\begin{aligned} P_{Br(I)} &\propto n_e (n_i + \sum_I n_I Z_I{}^2) \\ &\propto (n_i + \sum_I n_I Z_I) (n_i + \sum_I n_I Z_I{}^2) \\ &\propto n_e{}^2 Z_{eff} . \end{aligned} \tag{2.4}$$

The effective atomic charge Z_{eff} is defined by

$$Z_{eff} \equiv \frac{(n_i + \sum_I n_I Z_I{}^2)}{n_e} . \tag{2.5}$$

If only one kind of impurity occurs, we find from (2.2) and (2.4):

$$P_{Br(I)} / P_{Br(DT)} = 1 + f_I Z_I (Z_I + 1) + f_I{}^2 Z_I{}^3 . \tag{2.6}$$

For example a plasma with an impurity content of 3% of oxygen ($Z_I = 8$) has $P_{Br(I)} / P_{Br(DT)} = 3.6$, and for a plasma contaminated by 1‰ of iron ($Z_I = 20$), $P_{Br(I)} / P_{Br(DT)} = 1.4$. It follows from these examples that even very small amounts of impurities may cause a large increase of free-free radiation losses. Therefore it is of great importance to gain an insight into the amounts of impurities in the tokamak plasma. Spectroscopy can be an important diagnostic tool to achieve this insight.

Plasma-wall interaction

The main source of impurities is the plasma-wall interaction. Radiation and particle fluxes release molecules adsorbed at the walls and damage the internal structures by physical and chemical sputtering processes [*Boge-93*]. This causes contamination of the plasma by light ions like boron, carbon and oxygen, respectively metal ions like iron, nickel and chromium. Typical values for the impurity concentrations in the edge plasma are a few percent for light impurities and less than 10^{-2} percent for metal impurities. The metal concentrations increase with the plasma current and decrease with the electron density. The light impurity concentrations depend to a large extend on the state of the vacuum vessel and the size and position of the plasma [*Behr-85*].

There are several ways to control the contamination. A material limiter constricts the most outer closed magnetic surface, preventing the plasma-particles from reaching the wall. It follows from (2.6) that the bremsstrahlung-losses dramatically increase with increasing ion charge. Therefore walls, limiter, antennas et cetera are covered with light elements like carbon ($Z_C = 6$), boron ($Z_B = 5$) or beryllium ($Z_{Be} = 4$). It is even possible to cover them each with a different element. This allows identification of their individual contributions. The inner side of RTP is boronised. A material limiter has the disadvantage that the plasma-limiter interaction is still left. We can avoid this problem by using a magnetic limiter (so-called divertor, not at RTP). It also reduces the influx from particles released from the wall by removing them via the so-called scrape-off layer. A divertor also causes a better confinement of the plasma particles, but an even better confinement of the impurities because of their smaller cyclotron radii. This can cause an accumulation of impurities (often carbon), leading to a dramatic increase of radiation losses. We can avoid this problem by using the lower-Z elements B or Be instead of C as wall covering. Finally we can reduce the impurity concentrations by simply diluting them by increasing the plasma density.

Line radiation

In spectroscopy we make use of the line radiation the tokamak plasma emits when an excited electron in an atom or ion makes a transition to a less excited state. The energy is often expressed in m^{-1}, the unit of the wave number σ:

$$\Delta E(p,q) = hf = hc/\lambda = hc\sigma, \tag{2.7}$$

where $\Delta E(p,q)$ is the energy difference between the transition levels p and q, f the frequency, λ the wavelength and c the velocity of light. This is because Planck's constant h is not known

with an accuracy comparable to the very high accuracy of wavelength (and therefore wave number) measurements.

There are several types of emission processes. As mentioned before, in the centre of a tokamak plasma all low-Z atoms like hydrogen are fully ionised and do not emit any line radiation. Only at the outside of the plasma the temperature is low enough (several tens of eV) for low-Z ions to be not fully stripped and thus to emit line radiation following electron impact excitation.

For higher Z-ions, higher temperatures are required to cause ionisation. These higher temperatures occur more inside the plasma. We get a shell-like structure, where an ionisation stage has its density maximum lying more inside the plasma as the ionisation energy increases [*Wess-87*]. For example oxygen: the spectrum of neutral oxygen O I [1] is emitted by the relatively cold outer side. Going inside we "pass" the spectra of O II, O III and so on, until O VIII at $\hat{T}_e \geq 250$ eV. Fully stripped oxigen emits no line radiation (except by charge exchange processes like $O^{8+} + H \rightarrow O^{7+*} + H^+$). In the centre of the plasma only the small fraction of high-Z impurity ions like Fe, Ni and Cr emits line radiation. The multiply ionised impurity ions in the core plasma emit mainly in the VUV region. The Normal Incidence Spectrometer covers the wavelength region from 35 mn to 400 nm and is therefore well suitable to explore the behaviour of the impurity ions in the core.

Charge exchange processes with neutral particles created by plasma ions neutralised and reflected at the walls (e.g. $C^{6+} + H \rightarrow C^{5+*} + H^+$) can also cause emission of line radiation. For quantitative spectroscopy, this passive charge exchange radiation is considered to be the most difficult to take into account.

In active charge exchange spectroscopy, we "create" line radiation by injecting neutral particles into the plasma by means of neutral beam injection (not at RTP) or pellet injection. Charge exchange interaction with the injected neutral particles causes the ions in the plasma core to emit line radiation. Subtracting techniques can be used to separate the contributions of the active charge exchange emission from the core, from the passive emission from the parts of the plasma edge that are inevitably lying in the line of view of the spectrometer [*Boge-93, Hell-94*].

[1] In spectroscopy, the ionisation state is often indicated by a Roman number, e.g. O I means the neutral oxygen atom, O II the one times ionised atom, etcetera.

2.1.2 A transport-corona model

A plasma in thermodynamic equilibrium obeys several statistical laws. The Boltzmann distribution function

$$\frac{n(p)}{n(q)} = \frac{g(p)}{g(q)}\, e^{-\Delta E(p,q)/kT} \tag{2.8}$$

expresses the density $n(p)$ of an excited level p compared to the density $n(q)$ of another higher or less excited level q. In this formula, $\Delta E(p,q)$ is the energy difference between the two levels and $g(p) = 2J + 1$ is the quantum statistical degeneration for the level p, with J being the quantum number for the total angular momentum. We can use (2.8) to express $n(p)$ compared to the corresponding atomic or ionic ground level density $n(Z)$ by taking $q = Z$. The Saha equation (2.9) gives a relation between $n(p)$, the density $n(Z+1)$ of the ground level of the next higher ionisation stage and the electron density n_e:

$$\frac{(n(Z+1)/g(Z+1)) \cdot (n_e/g_e)}{n(p)/g(p)} = \left(\frac{2\pi m_e kT}{h^2}\right)^{3/2} e^{-\Delta E(p,Z+1)/kT}. \tag{2.9}$$

Again $g(Z+1)$, $g(p)$ and g_e are quantum statistical weight functions, and $\Delta E(p,Z+1)$ is the energy difference between the level p and the following ion ground level. With these laws we can calculate $n(Z)$, $n(Z+1)$, n_e and T_e from the density $n(p)$, which can be found from the line intensities.

However, a tokamak plasma is, as most plasmas, characterised by energy losses, temperature and density gradients and so on, and is nót in thermal equilibrium, not even in local thermal equilibrium. This means that the Boltzmann function and Saha equation do not hold. For calculating densities of excited levels we will have to use a model that corrects for deviations from these equations.

Continuity equations

Fast transport parallel to the magnetic field lines distributes the impurities homogeneously over the magnetic surfaces. The radial transport is much slower. The radial flux $\Gamma(Z)$ of atoms or ions in the ground level obeys the following continuity equation in cylindrical coordinates:

$$\frac{\partial n(Z)}{\partial t} = \frac{1}{r}\frac{\partial}{\partial r}(r\,\Gamma(Z)) + \left[\frac{\partial n(Z)}{\partial t}\right]_{cr}. \tag{2.10}$$

The term on the left hand side is the time-dependent term. The first term on the right-hand side is the transport term. The second term takes account for the gain and losses of particles by *c*ollision and *r*adiation processes. Similar we can write the continuity equations for the excited level p and the ground level of the next higher ionisation stage $Z+1$:

$$\frac{\partial n(p)}{\partial t} = \frac{1}{r}\frac{\partial}{\partial r}(r\,\Gamma(p)) + \left[\frac{\partial n(p)}{\partial t}\right]_{cr} \tag{2.11}$$

$$\frac{\partial n(Z+1)}{\partial t} = \frac{1}{r}\frac{\partial}{\partial r}(r\,\Gamma(Z+1)) + \left[\frac{\partial n(Z+1)}{\partial t}\right]_{cr} . \tag{2.12}$$

To explain the meaning of the collision-radiation terms, consider for example an atom or ion in the ground level, getting excited to a level p. It will be taken into account as "lost" in the collision-radiation term of (2.10) and as "gained" excited atom in the term of (2.11).

We assume that the densities of the excited levels are only influenced by collision and radiation processes and not by transport processes, the so called Quasi Steady State (QSS) approximation. Transport processes only indirectly influence $n(p)$, via $n(Z)$ and $n(Z+1)$. In our QSS approximation we suppose that $n(p)$ is a momentaneous function of $n(Z)$ and $n(Z+1)$; a plausible statement when considering the time scales of the concerning processes: assuming a transport velocity of $\sim 10^3$ ms^{-1} a particle can travel a characteristic distance of one centimetre in 10^{-5} s, which is much longer than the time for collision (typically $\sim 10^{-6}$ s) and radiation decay processes ($\sim 10^{-8}$ s) [*Hutc-90*]. Most time dependencies in a tokamak plasma, e.g. sawtooth-instabilities ($\sim 10^{-3}$ s), occur also on a time scale several orders of magnitude longer than the collision and radiation processes.

Because $n(p) \ll n(Z)$ and $n(Z+1)$, the terms in (2.11) are numerically small compared to those in (2.10) and (2.12), except for the collision-radiation term, which is equally large in all three equations. Therefore only in (2.11) the time-dependent term and the transport term are negligible small comparing to the collision-radiation term. Assuming a Maxwellian velocity distribution, the principle of detailed balancing states that the total number of collision and radiation processes equals the number of corresponding processes in opposite direction, because of their equal probabilities. Therefore the collision-radiation term in (2.11) equals zero:

$$\left[\frac{\partial n(p)}{\partial t}\right]_{cr} = 0 \tag{2.13}$$

In the corona model, we will consider this equation in a more explicite form, and see which collision and/or radiation terms are negligibly.

Corona equilibrium

The following equation holds for $[\partial n(p),\partial t]_{cr}$:

$$\left[\frac{\partial n(p)}{\partial t}\right]_{cr} = n_e \sum_{q\neq p} n(q)\, K(q,p) \quad - n_e\, n(p) \sum_{q\neq p} K(p,q)$$
$$+ \sum_{q\neq p} n(q)\, \Lambda(q,p)\, A(q,p) \; - n(p) \sum_{q\neq p} \Lambda(p,q)\, A(p,q), \qquad (2.14)$$

where Λ, the so-called escape factor ($0 < \Lambda < 1$), is a correction coefficient for reabsorbtion of radiation. $A(p,q)$ is the transition probability for the transition from p to q. The collision coefficient $K(p,q)$ is defined as the product of the cross-section $\sigma(p,q)$ for the collisional transition from p to q and the electron velocity v_e, integrated over the (Maxwellian) velocity distribution $f(E)$:

$$K(p,q) \equiv <\sigma(p,q)\, v_e> \equiv \int \sigma(p,q,E)\, v_e\, f(E)\, dE\,. \qquad (2.15)$$

The terms on the right hand side of (2.14) indicate successively the contributions of collisional (de)excitation from level q to level p (first term) and from p to q (second term), and radiative (de)excitation from q to p (third term) and from p to q (last term). Taking $q = Z+1$ we take collisional and radiative ionisation and recombination into account. With $q = Z$ we have the processes involving the ground level. In equilibrium follows from (2.13) that the right hand side of (2.14) equals zero.

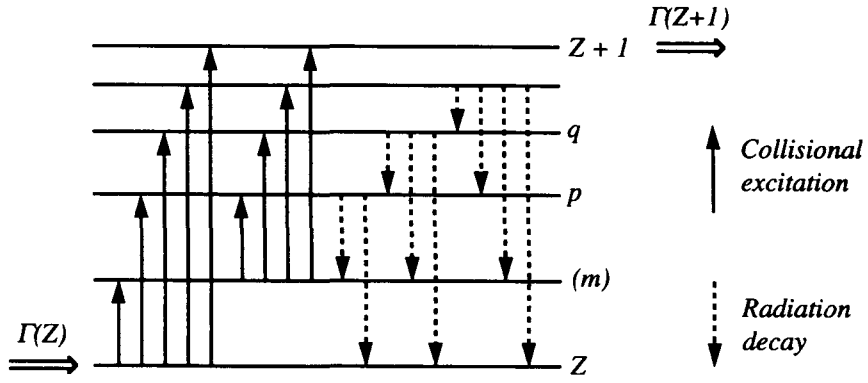

Figure 2.1 - The corona equilibrium is characterised by collisional excitation from the ground level (Z) and metastable levels (m) when existing, and deexcitation mainly by radiation processes. Losses of ions by transport processes dominate the losses by recombination. Transport processes only indirectly influence the densities of the excited levels, via ground level n(Z) and ground level n(Z+1) of the next higher ionisation stage.

For tokamak plasmas, the corona model is a useful approximation (figure 2.1). Due to the relative low n_e values (~10^{20} m^{-3}), we find a balance that is characterised by collisional excitation from the ground level and metastable levels, and deexcitation mainly by radiation processes. Losses of ions by transport processes are much more important than the losses by recombination. Therefore we neglect collisional and radiative recombination in our model by excluding $q = Z+1$. This reduces (2.14) to:

$$\left[\frac{\partial n(p)}{\partial t}\right]_{cr} = n_e\, n(Z)\, K(Z,p) + \sum_{Z+1>q>p} n(q)\, \Lambda(q,p)\, A(q,p)) - n(p) \sum_{q<p} \Lambda(p,q)\, A(p,q)) = 0 . \qquad (2.16)$$

It follows from this equation and the Boltzmann function that

$$n(p) = \frac{n_e\, n(p)\, K(p,Z) + \sum_{Z+1>q>p} n(q)\, \Lambda(q,p)\, A(q,p)}{\sum_{q<p} \Lambda(p,q)\, A(p,q)} . \qquad (2.17)$$

When we know the values for $K(p,Z)$, $A(q,p)$ and $A(p,q)$, we can use this equation and the Boltzmann function (2.8) to relate the density of the ground level $n(Z)$ to the density of the excited level $n(p)$ and the electron temperature T_e.
We can get a more accurate, but of course also more complicated model, by taking all terms of (2.14) into account. That means, two and more step ionisation, collisional deexcitation, radiative excitation and collisional and radiative recombination are also taken into account [*Boge-93*, *Isle-84* and others].

Charge exchange processes

Our model regards only collisional ionisation by electrons. Further improvement of the model can be achieved by also including charge exchange processes (§2.1.1). Consider the charge exchange reaction $X^{(Z+1)+} + H \rightarrow X^{Z+*} + H^+$ with the neutral hydrogen atoms in the plasma. We can take the loss of $X^{(Z+1)+}$ ions into account in formula (2.12) by adding a term

$$- n(Z+1)\, n_H < \sigma^{cx}\, v > . \qquad (2.18a)$$

In this formula n_H is the density of neutral hydrogen atoms and $< \sigma^{cx}\, v >$ denotes the average over the product of the cross-section for charge exchange and the relative velocity. Similar we can add a term

$$n(Z+1)\, n_H < \sigma^{cx}\, v > \qquad (2.18b)$$

to formula (2.10), in order to take the gain of X^{Z+} ions into account. Although n_H is small ($\sim 10^{15}$ m^{-3} at the plasma edge) comparable to the electron density n_e, the cross-sections for charge exchange reactions are relatively large. For example for the reaction $C^{5+} + H \rightarrow C^{4+*} + H^+$, $\sigma_{CV}^{cx} \approx 2.5 \cdot 10^{-19}$ m^2 and for $O^{5+} + H \rightarrow O^{4+*} + H^+$, $\sigma_{OV}^{cx} \approx 3.5 \cdot 10^{-19}$ m^2 at an energy of 1 keV. Therefore, in many circumstances charge exchange reactions cannot be ignored, especially for light elements [*Isle-84*].

Impurity transport

If the radial fluxes $\Gamma(Z)$ and $\Gamma(Z+1)$ are negligibly small, the steady state corona model yields the shell-like structure mentioned in paragraph 2.1.1. But especially the edge plasma is characterised by diffusion processes and influx of paricles from the walls (§2.1.1), and the steady state model will not hold. We can considerably improve our model by bringing the radial fluxes into account, by taking

$$\Gamma(Z) = -D \frac{\partial n(Z)}{\partial r} + n(Z)\, v \qquad (2.19)$$

in formula (2.10). Similar we can change formula (2.12). The first term on the right-hand side of (2.19) expresses the diffusion of neutral particles into the plasma, where D is the diffusion coefficient. The second term is a convection term. For the convective flow velocity v, the expression $-v_0 r / a$ is often used, where v_0 is the convective flow velocity at the plasma edge, r is the radial co-ordinate and a the minor axis of the torus [*Wess-87*]. Reported experimentally values are 1 m^{2}s^{-1} for diffusion coefficient D and 1-10 ms^{-1} for v_0 [*Behr-86*]. We now can relate the total density of an ionisation state to the influx of neutrals.

Experiments showed that both diffusion coefficient and convective flow velocity are anomalously large as compared with theory. To explain these anomalies, it is believed that both electrostatic turbulences, connected to electron density fluctuations, and magnetic turbulences have to be taken into account. Fluctuating electric fields can cause particle drifts and convection across magnetic surfaces. Magnetic turbulences can destroy the magnetic topology, causing enhanced transport of plasma particles along the perturbed field lines. On a more elementary level we can say that the several turbulence effects influence time scale and length scale of the particle collisions as compared to theoretical predictions [*Koni-94*].

The ratio $v_0 a / D$ determines the strength of the peaking of the radial density profile of an ionisation stage. High transport fluxes lead to a broadening of the shells, and shifts their maxima to higher temperatures. By measuring the shells using spatial scan spectrometers like the NIS, we could verify the transport-corona model. More refined transport models can be found in the literature [*Lack-82*, *Koni-94*].

2.2 Grating spectroscopy

Light of wavelengths below 200 nm is absorbed by air, so spectroscopy in this region has to be done in vacuum. Therefore this wavelength region is called the Vacuum Ultra Violet (VUV) region. Below 100 nm, the so called far ultra violet region, there are no transparent media. Hence optical systems for these wavelengths are built with reflective components. Because the reflectivity becomes poorer for lower wavelengths, one will try to use as few reflective components as possible. Therefore a VUV-spectrometer is usually built with a concave spherical grating as a both diffracting and focusing element. The NIS is equipped with two interchangeable concave spherical gratings. For wavelengths below 50 nm the reflectivity of all materials has dropped to only a few percent. In this region we have to use grazing incidence spectrometers like the RIS. They are based on the fact that for very large angles of incidence the reflectivity approaches unity for all wavelengths. Below 20 nm, the VUV region overlaps with the soft X-ray region, and here both optical and X-ray methods can be applied.

2.2.1 Concave spherical grating

In the ideal situation a concave spherical reflection grating diffracts the light coming from the narrow entrance slit and focuses a series of images - the spectrum - on a detector, e.g. a photo-electric camera or photographic plate. Slit, grating and camera are all on the Rowland circle. In figure 2.1 the camera is positioned at the first order image.

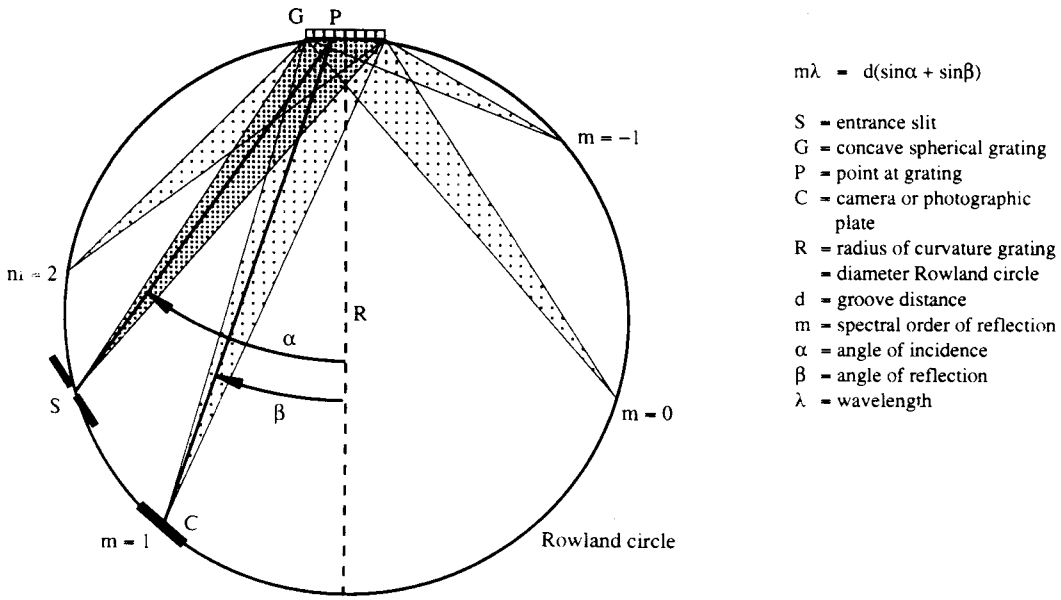

Figure 2.2 - The Rowland circle as an approximation of the real focal curve of a concave spherical grating.

Consider the light reflected at a point P of the grating (see figure 2.1). The optical path is defined by

$$F = SP + PC + Nm\lambda . \tag{2.20}$$

In this formula N is an integer. The other symbols are explained in the figure. The last term expresses that F increases an integral number of wavelengths when we go from one groove to the next. When we express SP and PC in cylindrical co-ordinates and expand them into a power series, we get an expression for the optical path of the following form [*Beut-45*]:

$$F = F_1 + F_2 + F_3 + F_4 + F_5 + F_6 + \ldots \tag{2.21}$$

Applying Fermat's principle (constant optical path length) on F_1 leads to the grating equation:

$$m\lambda = d(\sin\alpha + \sin\beta). \tag{2.22}$$

At the same way we find the Rowland circle as focusing condition from F_2:

$$\begin{cases} PS = R\cos\alpha \\ PC = R\cos\beta \end{cases} . \tag{2.23}$$

In practice the groove distance d is not constant across the grating. When taken into account a linear varying groove distance as a first order approximation, we find the following more realistic focusing condition:

$$\begin{cases} PS = \dfrac{R\cos^2\alpha}{\cos\alpha + \varepsilon\sin\alpha} \\ PC = \dfrac{R\cos^2\beta}{\cos\beta + \varepsilon\sin\beta} \end{cases} . \tag{2.24}$$

The coefficient ε expresses the deviations between this Ω-shaped self focussing curve and the Rowland circle of formula (2.23). For large spectrometers these deviations can be of the order of centimetres. The deviation is the smallest for low angles of incidence. Typically $\varepsilon \sim 10^{-4}$ - 10^{-6}. For an ideal grating ε becomes zero. Formula (2.24) then gives the Rowland circle as an ideal case of the self-focusing curve.

The remaining terms of (2.21) express several kinds of aberrations of the grating. F_3 has the meaning of astigmatism: a point on the slit will be imaged as a line perpendicular to the focal plane. When not compensated this can cause loss of light, especially for grazing incidence spectrometers. F_4 expresses coma and line curvature. Coma can be neglected when the deviations between focal curve and Rowland circle are small. Line curvature does not play an important role as long as we don't come too close to the grating, compared with its dimensions. F_5

gives the spherical aberration. It can only be controlled by limiting F_5 to a quarter of a wavelength by limiting the diameter W of the grating:

$$W \leq 2.38 \left(\frac{\lambda R^3 \cos\alpha \cos\beta}{(1 - \cos\alpha \cos\beta)(\cos\alpha + \cos\beta)} \right)^{1/4} . \tag{2.25}$$

Finally, F_6 vanishes when focusing on the Rowland circle. A more detailed description on concave spherical grating theory can be found in [*Beut-45, Meij-87, Sai-68*].

Blazed gratings

One of the main disadvantages of a grating spectrometer is that the available light is spread out over the various orders, producing overlapping spectra. For a normal grating most of the incident light undergoes specular reflection, corresponding to the zeroth order. This light is useless for spectroscopy, since the constituent wavelengths overlap and no spectrum occurs. By using gratings with grooves with a controlled shape, so called blazed gratings, we can concentrate the reflections into a well defined order.

2.2.2 Resolving power

The resolving power of a grating spectrometer is defined by

$$\mathcal{R} \equiv \frac{\lambda}{\Delta\lambda} , \tag{2.26}$$

in which $\Delta\lambda$ is the smallest resolvable wavelength difference and λ is the mean wavelength. $\mathcal{R}$ is determined by three factors. First there is the resolving power of the grating, given by

$$\mathcal{R}_g \equiv \frac{\lambda}{\Delta\lambda_g} = \frac{mW}{d} = mN . \tag{2.27}$$

In this formula, m is the spectral order of reflection, W the (effective) width of the grating, d the groove distance and N is the number of grooves. Using the grating formula (2.22) we can get rid of the order of reflection:

$$\mathcal{R}_g = \frac{W(\sin\alpha + \sin\beta)}{\lambda} . \tag{2.28}$$

The resolving power also depends on the spatial resolution Δc of the camera or photographic plate. Again using the grating formula, we can derive the angular dispersion

$$\frac{d\beta}{d\lambda} = \frac{m}{d\,cos\beta}. \tag{2.29}$$

For the reciprocal linear dispersion at the camera, the so-called plate factor, we find as first order approximation (β small):

$$\frac{\Delta\lambda}{\Delta c} \approx \frac{d\,cos\beta}{mR} = \frac{\lambda\,cos\beta}{R\,(\,sin\alpha + sin\beta\,)}, \tag{2.30}$$

so we find as resolving power of the camera:

$$\Re_c \equiv \frac{\lambda}{\Delta\lambda_c} = \frac{m\lambda\,R}{d\,cos\beta\,\Delta c} = \frac{R\,(\,sin\alpha + sin\beta\,)}{cos\beta\,\Delta c}. \tag{2.31}$$

Finally, the resolving power depends on the width of the slit Δs : a smaller slit gives a higher resolving power, but of course also a less amount of light. We find a similar formula as for the camera:

$$\Re_s \equiv \frac{\lambda}{\Delta\lambda_s} = \frac{R\,(\,sin\alpha + sin\beta\,)}{cos\beta\,\Delta s}. \tag{2.32}$$

In fact, we should multiply (2.32) by some projection factor, but as $SP \approx PC$ in figure 2.2, this factor is nearly one. It follows directly from (2.31) and (2.32) that a larger radius of curvature R gives a higher resolving power. This leads to very large spectrometers like the NIS. We can get an indication of the resulting resolving power of a spectrometer by using

$$\Delta\lambda = \sqrt{\Delta\lambda_g^{\,2} + \Delta\lambda_c^{\,2} + \Delta\lambda_s^{\,2}} \tag{2.33}$$

in formula (2.26).

2.3 Spectroscopic analysis

2.3.1 Impurities

Impurity ions can be determined by their characteristic spectral emission lines. As mentioned in paragraph 2.1.1, the most important impurity ions to be expected in the RTP tokamak plasma are the light impurities boron, carbon and oxygen, and metal impurities like iron and nickel. Ionisation states having complicated electronic structures with 3d-electrons like Fe I are often difficult to detect above the background, as the spectral emission is spread over many lines. Strong spectral lines of several ionisation states of these elements within the region 35 nm - 400 nm are listed in appendix 1. Some strong hydrogen lines are also given. Mainly resonance lines lines are listed, as we will concentrate our measurements on these.

To get an indication of the resolving power needed to resolve the fine structure splittings, consider the five B I lines at 137 nm as marked in table A1.2. Neglecting effects like Doppler broadening (§2.3.4), we need a resolving power

$$\Re \equiv \frac{\lambda}{\Delta\lambda} \geq \frac{137.9}{0.0023} \approx 60{,}000 \tag{2.34}$$

to resolve all five lines. With a detector pixel size of 14 μm, the NIS provides a resolving power of 120,000 at these wavelengths (§3.1), well enough to resolve the lines.

2.3.1 Line intensity measurements

The intensity of the spectral line resulting from the transition from a level p to a level q is given by

$$I(p,q) = \frac{hc\sigma}{4\pi} \frac{g(p)}{g(q)} A(p,q)\, n(p) \ . \tag{2.35}$$

In this formula h is Planck's constant, c the velocity of light, σ the wave number, $g(p)$ and $g(q)$ are quantum statistical weight functions, $n(p)$ is the density of the upper level p and $A(p,q)$ is

the transition probability, given by

$$A(p,q) = f(p,q)\,\frac{2\pi e^2 \sigma^2}{\varepsilon_0 m_e c}$$

$$= \frac{16\pi^3 e^2 \sigma^3 |r_{pq}|^2}{3h\,\varepsilon_0}, \qquad (2.36)$$

in which e is the electron charge, m_e the electron mass, ε_0 the permittivity in vacuum, $f(p,q)$ is the oscillator strength and r_{pq} the matrix element of the dipole oscillator for the transition $p \rightarrow q$ [*Sijd-92*]. As an indication, in the ultra violet region $A(p,q)$ is in the order of 10^9.

Electron temperature and density

We can determine a relation between the electron temperature T_e and the electron density n_e from the intensity ratios of spectral lines of the same species, by combining the latter two formulas with formula (2.17). We can now calculate T_e when n_e is known and inversely. It is also possible to extract both T_e and n_e simultaneously from a spectrum when using two or more line intensity ratios with a different dependence on T_e and n_e [*Boge-93*, *Hutc-90*, *Zast-91*]. When both T_e and n_e are known from an independent diagnostic (difficult at the plasma edge), e.g. a Thomson scattering diagnostic, we can use the relation between T_e and n_e to verify our model. However, there are some difficulties. The electron temperature and density vary across the observation volume, especially for line integrated measurements. As will be described in chapter three, the NIS is equipped with a scanning mirror system, which provides some focusing at a small area in the plasma. This will probably reduce the problem. Another issue is that whereas the coefficients $A(q,p)$ and $A(p,q)$ are well known in many cases, the coefficients $K(p,Z)$ are often hard to predict, because all mechanisms have to be known. Ionisation rates as calculated by Lotz are often used [*Isle-84*, *Lotz-68*].

Ion densities and influx of particles

Combining (2.35) and (2.36), we can determine the density $n(p)$ of the excited level p from the absolute spectral line intensity. Using the equations (2.8) and (2.17), we can relate $n(p)$ to the density of the atomic or ionic ground level $n(Z)$. The radial influx of (neutral) particles entering the plasma can be calculated by using (2.19). Besides the necessary absolute calibration of the spectrometer, the difficulties mentioned above also remain. Cross-checking can be done with Z_{eff} measurements, e.g. from bolometry or current density measurements.

Absorption spectroscopy

A more direct way to measure atomic and ionic ground level densities is by using absorption techniques. In absorption spectroscopy we pass light through the plasma and measure the absorption lines. Again they are characteristic for the ions and atoms in the plasma. As far as known, no VUV absorption spectroscopy has ever been done on tokamak plasmas, so this could be a very interesting issue for the NIS.
We can use continuum UV light sources like BRV (Ballofet, Romand, Vodar) sources or laser produced plasmas [*Mei2-87*]. It is also possible to use a laser as light source. Then we can do very selective measurements by tuning its frequency on a selected absorption line. It also allows a very high spatial resolution. A disadvantage is that most lasers are only tuneable over a very limited wavelength range, leaving many unobservable gaps in the range one wishes to cover.

2.3.3 Plasma rotations

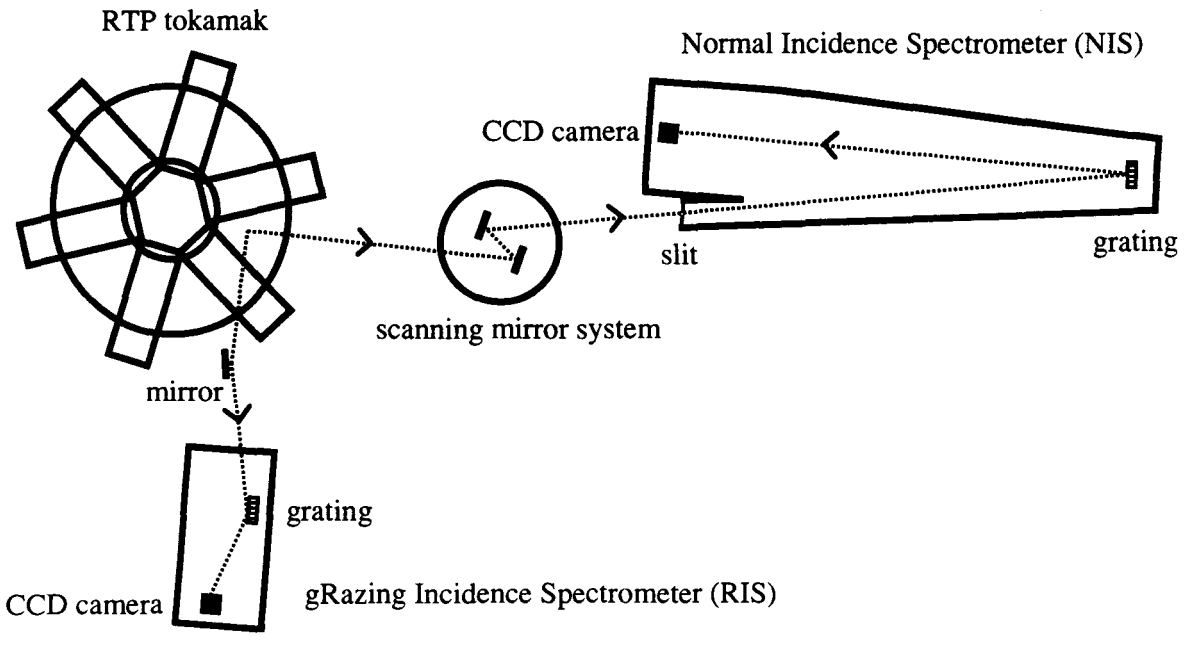

Figure 2.3 - Location of the NIS and the RIS spectrometer at the tokamak.

The plasma shows rotations in toroidal direction. Rotations in poloidal direction have also been reported. It has been suggested that both rotations act as two coupled oscillations, that means, the toroidal rotational kinetic energy is transferred into poloidal rotational

kinetic energy and backward. We can measure these non-turbulent macroscopic movements by using the Doppler frequency shift they cause. The combination of the NIS (Normal Incidence Spectrometer) and the RIS (gRazing Incidence Spectrometer), which will become operational later this year, allows for simultaneous measurement of both rotations at the same location in the plasma (see figure 2.3). The NIS with its radial line of sight will be able to measure the poloidal rotation velocity. The RIS is viewing in toroidal direction at the same point in the plasma.

Doppler frequency shift

When a photon is emitted by an impurity ion moving with a velocity v at an angle θ to the line of sight of the observer, its frequency f is Doppler shifted by

$$f = f_0 \frac{1 - (v \cos\theta / c)}{(1 - (v / c)^2)^{1/2}} \approx f_0 (1 - \frac{v}{c} \cos\theta) \quad (c \gg v). \tag{2.37}$$

In this expression, f_0 is the frequency emitted by a non moving ion and c is the velocity of light. We can use this Doppler frequency shift to measure plasma velocities. To be precisely, we measure the velocities of the emitting impurity ions that are moving along with the other plasma particles, using them as a diagnostic tool. It is even possible to dilute the plasma on purpose for diagnostic reasons, e.g. with helium or neon.
From (2.37) we find for the relative Doppler frequency shift

$$\frac{\Delta f}{f_0} \equiv \frac{f - f_0}{f_0} \approx \frac{v}{c} \cos\theta . \tag{2.38}$$

Taking $\theta = 0$ we get for the relative wavelength and wave number shift

$$\frac{\Delta\lambda}{\lambda} = \frac{\Delta\sigma}{\sigma} \approx \frac{v}{c} . \tag{2.39}$$

As a rule of thumb, it follows from (2.39) that the minimum speed we can measure with a spectrometer having a resolving power $\mathfrak{R}$ (formula (2.26)) is given by

$$v \geq \frac{3 \cdot 10^8}{\mathfrak{R}} . \tag{2.40}$$

For the normal incidence spectrometer (NIS), which has a resolving power up to 400,000 (§3.1.3), we find a minimum speed of about 750 ms^{-1} (!).

2.3.4 Ion temperatures

The microscopic temperature movement of the emitting impurity ions also causes Doppler frequency shift, resulting in broadening of the spectral lines. Assuming a Maxwellian velocity distribution

$$N(v,T_I)\,dv \;=\; n\,(m_I / 2\pi kT_I)^{3/2}\,exp(-m_I v^2 / 2kT_I)\,dv\,, \tag{2.41}$$

we can calculate the intensity distribution as a function of the frequency f around the central frequency f_0 of the spectral line:

$$I(f) \;=\; I_0\,exp\,(-m_I c^2 (f - f_0)^2 / 2kT_I f_0^2)\,. \tag{2.42}$$

The Gaussian profile has a relative full width half maximum of

$$\frac{\Delta\lambda}{\lambda} = \frac{\Delta\sigma}{\sigma} = \frac{2}{c}\sqrt{\frac{2\ln 2 kT_I}{m_I}} \;\approx\; 2.44\cdot 10^{-3}\sqrt{\frac{\hat{T}_I\,[keV]}{A_I\,[amu]}}\,, \tag{2.43}$$

where A_I is the atomic mass number and $\hat{T}_I$ the ion temperature in keV.
What resolving power do we need to measure ion temperature $\hat{T}_I$ of an ion species with mass number A_I ? Provided that we spread out the line profile over at least ten detector pixels, we need a resolving power

$$\Re \equiv \frac{\lambda}{\Delta\lambda} \;>\; 10\cdot 4.10\cdot 10^2\sqrt{\frac{A_I}{\hat{T}_I}}\,. \tag{2.44}$$

For example, for measuring oxigen (A_I = 16.00 amu) ion temperatures down to 10 eV, we need a spectrometer having a resolving power $\Re$ of at least 165,000. Again the extremely high resolving power of the NIS allows us to measure those low temperatures, that occur at the plasma edge.

Interpretation of ion temperatures

The Heisenberg uncertainty relation states that a spectral line has a certain minimum width, as the excited state has a finite lifetime. But high collision rates for the excited ions can shorten their effective lifetimes causing pressure broadening (Lorentz broadening). The presence of neighbouring charged particles can also cause Stark broadening. For tokamak plasmas however, both effects are usually negligibly.

Charge exchange reactions between hot ions and cold neutrals in the plasma edge can transfer into cold ions and hot neutrals. This could lead to a situation where we have a hot and a cold ion temperature component in the plasma edge [*Hey-94*].
It has been reported [*Hell-94*] that the temperatures measured at the outside of the plasma are higher than expected. There are several disturbing effects that could explain these and other possible deviations. Sheer of toroidal respectively poloidal velocities across the observation volume could cause an extra Doppler broadening of the spectral lines. The NIS/RIS combination discussed in paragraph 2.3.3 could be helpful in proving this statement. The electrostatic and magnetic turbulences mentioned in §2.1.2 could also disturb the Doppler temperature measurements. Further, the confining magnetic field in a tokamak can cause an extra broadening. These Zeeman and Paschen-Back effects will be discussed in paragraph 2.3.5. Finally there are of course the limitations of the used spectrometer, which has a finite resolving power. Two close lying lines may appear as one broadened line.

Asymmetric profiles

In the plasma edge most particles move inwards, giving the radial influx described in paragraph 2.1.2. This often causes asymmetry of the Gaussian intensity profiles (2.42). The velocity distribution depends on the penetration depth of the atoms into the plasma, which in turn depends on the type of plasma-wall interaction. For example the particles released by desorbtion or chemical sputtering give narrower line intensity profiles than those reflected or physically sputtered. So the asymmetry of the profiles gives an indication of the interaction processes [*Boge-93*].

2.3.5 Magnetic field strength

The confining magnetic fields in a tokamak, about two Tesla at RTP, can cause a significant splitting of the degenerated energy levels into sets of Zeeman or even Paschen-Back components. We can use this effect to determine the magnetic field strength, again using the impurities as a diagnostic tool.
For light atoms and relatively weak magnetic fields, the total orbital angular momentum vector L and the total spin vector S remain coupled to form a total angular momentum vector J. The energy levels ${}^{2S+1}L_J$ are splitted into Zeeman components having a different magnetic quantum number m_J . In a first order approximation ($B < 10$ T) the splitting is proportional to the magnetic field strength:

$$\Delta E \approx m_J \, g_L \, \mu_B \, B \, . \tag{2.45}$$

In this formula μ_B is the Bohr magneton for the electron, defined by

$$\mu_B \equiv \frac{e\hbar}{2m_e} , \tag{2.46}$$

and

$$g_L \equiv 1 + \frac{J(J+1) + S(S+1) - L(L+1)}{2J(J+1)} \tag{2.47}$$

is the Landé factor. As a consequence of the splitting of the energy levels, a spectral line $hc\sigma = E_p - E_q$ will also be splitted into sets of Zeeman components

$$\begin{aligned} hc\sigma &= (E_p + \Delta E_p) - (E_q + \Delta E_q) \\ &= (E_p - E_q) + \mu_B B \, (\, [m_J g_L]_p - [m_J g_L]_q \,) \, . \end{aligned} \tag{2.48}$$

The wavelength difference between the components is given by

$$\Delta\lambda = \mu_B \, B \, \lambda^2 \, (\, [m_J g_L]_p - [m_J g_L]_q \,) \, / \, hc \, . \tag{2.49}$$

It follows from this formula that the Zeeman splitting is very small for short wavelengths.

The magnetic field in a tokamak is strong enough to cause significant Paschen-Back effects, for example in some C II and C III multiplets [*Hey-94*]. The L and S vectors are decoupled and the energy levels are splitted into Paschen-Back components with different $m_L + 2m_S$. Again the splitting is proportional to the magnetic field strength:

$$\Delta E = (m_L + 2m_S) \, \mu_B \, B \, . \tag{2.50}$$

The other formulas are also similar to those for the Zeeman effect and will not be discussed here [*Sho-68*].

For the Zeeman effect, we can discriminate between the normal effect, occurring for transitions between two levels both having $S = 0$ ($g_L = 1$ for both levels) and the more complicated anomalous effect when the Landé factor g_L is different from one for one or both levels. As the different Zeeman components of a spectral line are polarised, we can select between them by using filters. When the direction of observation is parallel to the magnetic field, we can select between the (groups of) circularly polarised σ components by using a quarter-wave plate with a linear polariser. When viewing perpendicularly to the magnetic field, we can select between the π and σ components by using a linear polariser.

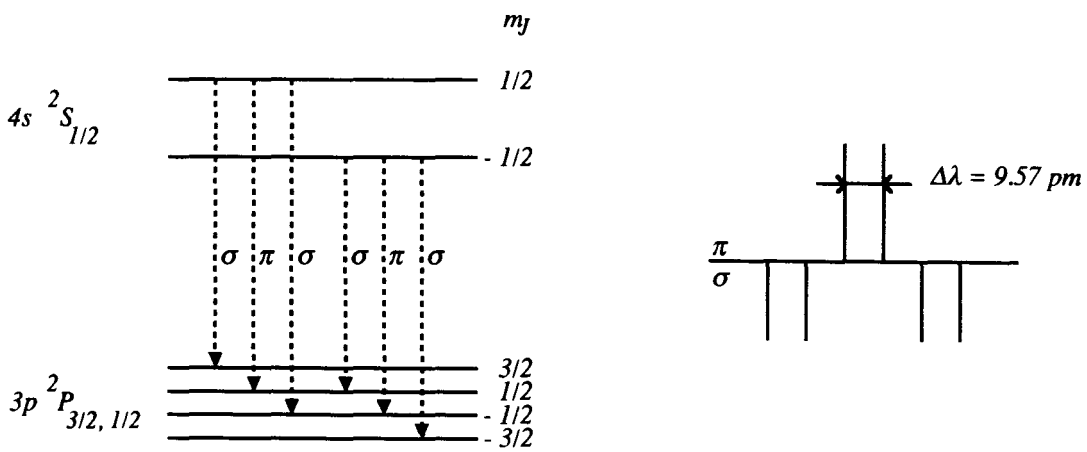

Figure 2.4 - Zeeman splitting of the 4s $^2S_{1/2}$ - 3p $^2P_{3/2,1/2}$ transition lines in C II.

To get an indication of the resolving power needed to resolve the Zeeman splittings, consider the C II transitions from the 4s $^2S_{1/2}$ singlet to the 3p $^2P_{3/2,1/2}$ doublet at 392 nm as marked in table A1.3. In the confining magnetic field the singlet is splitted into two and the doublet into four Zeeman levels. As a consequence, the two fine structure spectral lines are splitted into six lines, two π and four σ components (figure 2.4). Using formulas (2.46) till (2.49), we can calculate the wavelength difference between for example the two π components as 9.57 pm (0.0957 Å) in a 2 T magnetic field. To resolve them, we need a resolving power of

$$\mathcal{R} \equiv \frac{\lambda}{\Delta\lambda} \geq \frac{392}{0.00957} \approx 40{,}000\,, \qquad (2.51)$$

so the NIS will be able to resolve them. If the Doppler temperature broadening (§ 2.3.4) of the Zeeman components is of the same order of magnitude as the Zeeman splitting itself, it could

become difficult to resolve the overlapping broadened lines. We can deal with this problem by selecting a normal Zeeman splitted line, e.g. the $2s^2\ ^1S_0$ - $2p\ ^1P_1$ transition in C III (table A1.3). Such line is splitted in only one π component between two σ components. By a proper choice of filters and direction of observation, we can select a single Doppler broadened component and use it for temperature measurement.

More complicated line structures can be decomposed using mathematical techniques: we can calculate the positions (using the magnetic field strength as parameter) and the relative intensities [*Sho-68*] of the Zeeman components. The Doppler broadening profile given by formula (2.42) is the same for all components. The success of the decomposing depends to a large extend on the quality of the resolved complex line shapes. The NIS, with its resolving power up to 400,000, again will be a very useful instrument.

Chapter 3

The Normal Incidence Spectrometer (NIS)

The Normal Incidence Spectrometer (NIS) [*Klee-64*] has been moved from the Zeeman Laboratory of the Amsterdam University. Since its original commissioning, the photographic plate holder and the grating turret (§3.1) have been replaced by a complete new design [*Meij*]. At the FOM Institute we equipped the NIS with a Scanning Mirror System (SMS), providing two-dimensional scanning of the source point through the plasma. This means that we can do local measurements of ion species, temperatures, velocities, magnetical field strength et cetera, without the need for inversion techniques. As discussed in paragraph 2.3.3, the location of the NIS and the RIS will allow simultaneous measurement of poloidal and toroidal plasma rotations at the same point in the plasma. We implemented a CCD camera to do high temporal resolved (0.2 ms) measurements. To interpret the data, we developed a highly sophisticated set of programs. The large amounts of data are automatically reduced and stored in the central data management system for all RTP diagnostics. A graphical user interface provides fast and easy adjustment of the computer controlled optical system from any terminal. Further we improved the continuously operating vacuum system with a new control system. It prevents damage to the vacuum system and the optical system.

In this chapter we will discus the NIS more in detail. The first paragraph describes the optical system: the gratings, the detector, the theoretical resolving power and the SMS used to couple the light from the plasma into the spectrometer. Its very high resolution makes the NIS also very suitable for absorption spectroscopy. Paragraph 3.1.5 gives some suggestions. The vacuum system will be described in paragraph 3.2. Control and data-acquisition are discussed in paragraph 3.3. The last paragraph is about calibration and testing.

3.1 Optical system

3.1.1 Gratings

Figure 3.1 gives a schematic top view of the NIS. We can recognise the Rowland circle from figure 2.2.

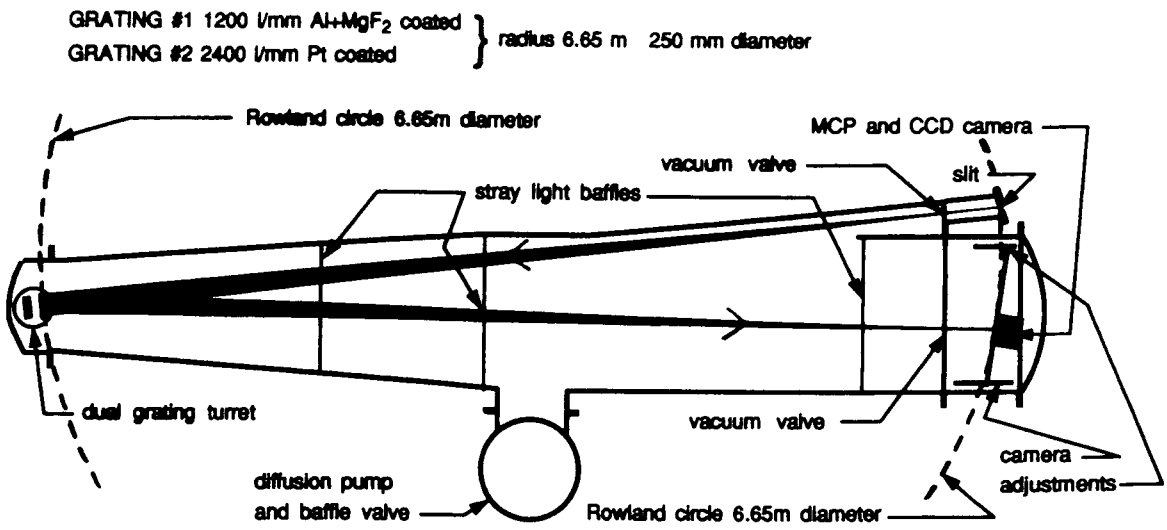

Figure 3.1 - Schematic view of the NIS.

The light is entering the spectrometer through the entrance slit, which has a width Δs of about 10 μm. A moveable mirror direct behind the slit (not in figure) allows us to branch off the light from the plasma when needed. Three screens, with apertures just big enough to pass the diffracted beam, intercept stray light from reflections at the inner walls of the vacuum tank. The NIS is equipped with two gratings, mounted on a turret. We can interchange them by turning the turret 180 degrees around its vertical axis. Together the gratings cover the wavelength region from 35 to 400 nm (35.4 - 3.1 eV). Table 3.1 gives a survey of the main parameters of the two gratings. Because the gratings have a round shape, we have to use the effective width W in our calculations, which is a factor 0.82 smaller than the diameter. The factor 0.82 results from the Rayleigh criterion for resolution (two neighbouring lines will be just resolved when the centre of one maximum falls on the first minimum of the adjacent line, i.e. the centres of the maxima are separated by half the width of the lines) applied to the Airy disk [*Long-73*].

Table 3.1 - The two gratings of the NIS.

Grating	*1*	*2*	-
Diameter	*250*	*250*	*mm*
Effective width (W)	*≈ 200*	*≈ 200*	*mm*
Focal length (R)	*6650*	*6650*	*mm*
Lines per mm (d^{-1})	*1200*	*2400*	*mm^{-1}*
Spectral range	*110 - 400*	*35 - 200*	*nm*
Blaze wavelength	*170*	*70*	*nm*
Coating	*$Al + MgF_2$*	*Pt*	-
Resolving power	*100,000 - 250,000*	*100,000 - 400,000*	-

We can scan part of the spectrum projected by the chosen grating, by moving the detector along the series of images. By limiting this linear displacement of the detector to a maximum of 100 mm, we keep the detector within the depth of field without rotation. In this way we cover a wavelength range of 12.5 nm (grating 1) respectively 6.25 nm (grating 2). We can select another part of the spectrum by turning the grating around its vertical axis. The mechanical construction allows adjustment of this grating angle in discrete steps of one degree, with a reproducibility better than $1 \cdot 10^{-6}$ degree (15 μm linear displacement at the detector, corresponding to a wavelength shift of 1.9 pm). In near future the angle-step will be decreased to one third of a degree. This is the first practically achievable value below 0.43°, the least necessary step to let the wavelength ranges covered by the detector overlap. Three precision actuators allow remote control of the changing of the gratings, the grating angle and the mentioned detector-displacement. Four more actuators allow as many other adjustments: both grating and detector can be moved into each others' direction in order to fulfil the positioning of slit and detector on the grating's Rowland circle. The detector can be turned around a vertical axis to keep it viewing towards the grating. Finally we can adjust the height of the camera. All adjustments can be performed between two plasma shots. More details about electronics and software can be found in [*Stek-93*].

3.1.2 Camera and multichannel plate

Figure 3.2 shows the construction of the detector. The light reflected by the grating is first amplified by a MultiChannel Plate (MCP, Photek). It consists of a large number of electron multiplier tubes (see inset), each having a diameter of 10 μm. The distance between the tubes is 12 μm. The MCP is coated with CsI and has a diameter of 25 mm. After being transferred into visible light by a phosphor screen, an optical system projects the spectrum on a Charge Coupled Device (CCD) camera.

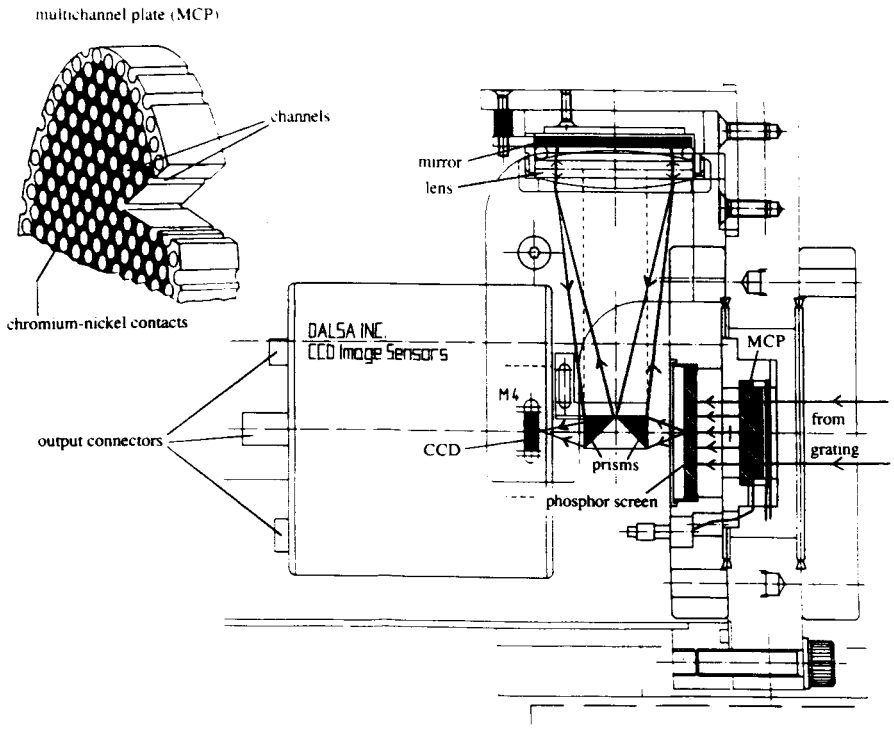

Figure 3.2 - Construction of the detector of the NIS. The light reflected by the grating is first amplified by a multichannel plate, consisting of a large number of electron multiplier tubes (inset). After being transferred into visible light by a phosphor screen, an optical system projects the spectrum on the CCD camera.

The CCD camera used (Dalsa) is specially designed for spectroscopy. It has 2048 rectangular shaped pixels (14 μm × 500 μm), to provide a maximum of light per pixel. The exposure time can be adjusted remotely between 0.2 and 825 ms. A fast 8 bit AD converter provides a maximum time resolution of 0.2 ms (5 frames per ms). This means that even fast phenomena like sawtooth oscillations (typical 1 ms) can be resolved. Table 3.2 gives a list of characteristics of the CCD camera.

Table 3.2 - Some characteristics of the CCD camera (DALSA).

Number of pixels	*2048*	-
Size of pixels (Δc)	*14 x 500*	*μm*
Exposure time	*0.2 - 825*	*ms*
Highest time resolution	*5*	*frames per ms*
Maximum number of frames	*1280*	*frames per shot*
Resolution AD converter	*8*	*bits*

3.1.3 Resolving power

Table 3.3 gives the theoretical resolving powers of the gratings ($\mathfrak{R}_g$), camera ($\mathfrak{R}_c$) and slit ($\mathfrak{R}_s$) for several wavelengths, calculated using the formulas of paragraph 2.2.2#. The total resolving powers ($\mathfrak{R}$) are also given. When using a high resolution photographic plate instead of a multichannel plate and a CCD camera and a matching smaller slit, the even higher resolving powers mentioned before can be reached. This off course at the expense of the time resolution, although we can select a time slice using a high speed shutter.

Table 3.3 - Theoretical resolving powers of the NIS for several wavelengths, when using the multichannel plate and CCD camera. Even higher resolving powers can be reached when using a high resolution photographic plate and a matching smaller slit.

Grating (lines/mm)	λ [nm]	$\mathfrak{R}_g$	$\mathfrak{R}_c$	$\mathfrak{R}_s$	$\mathfrak{R}$
1	400	240,000	235,000	329,000	150,000
1200	170	240,000	97,000	136,000	75,000
	110	240,000	63,000	88,000	50,000
2	200	480,000	235,000	329,000	178,000
2400	70	480,000	80,000	112,000	65,000
	35	480,000	40,000	56,000	32,000

3.1.4 Scanning Mirror System

A Scanning Mirror System (SMS) is used to measure the spectrum emitted by a well-defined part of the plasma, with a spatial resolution of about 1 cm (see figure 2.3). It consists of two moveable concave mirrors having focal lengths of f_1 = 4 m and f_2 = 2 m respectively. The square (10 × 10 cm) aluminium mirrors are coated with MgF_2 to protect them against oxidation. Their reflectivity in the region of interest is better than 80%. They project an image of a small part of the plasma on the entrance slit of the NIS. Each mirror has two degrees of freedom. This allows two-dimensional scanning of the source point through the plasma. Figure 3.3 gives a top view of the system.

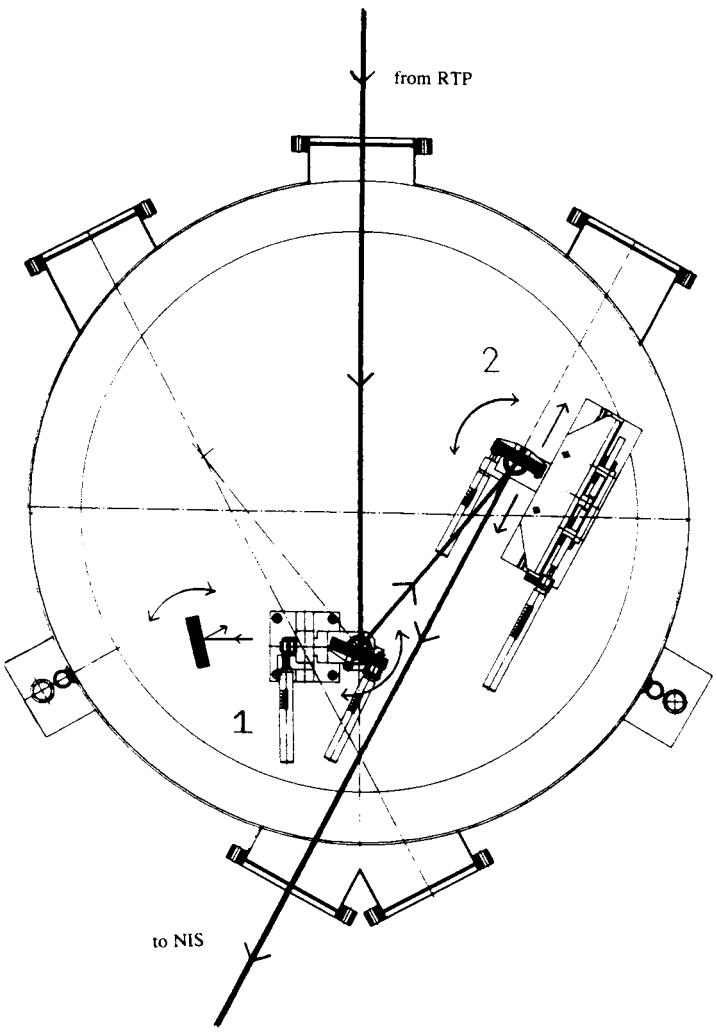

Figure 3.3 - The scanning mirror system used to couple the light of a well-defined part of the plasma into the NIS. The two concave mirrors provide a two-dimensional scan of the source point. See also appendix two.

By tilting mirror 1 around its horizontal axis, we can scan in vertical direction. The depth scan (radial direction) can be accomplished by the changing the distance between the two mirrors. This can be done by the linear movement of mirror 2. The mirrors can also be turned around their vertical axes to keep optical contact between them. The toroidal viewing line can be adjusted by turning mirror 1 around its vertical axis and will be fixed at a position minimising coma. This corresponds to a viewing line lying in a poloidal plane. Appendix two gives the relations between the co-ordinates of the source point in the plasma and the positions of the mirrors.

Four high precision actuators allow remote adjustment of the mirrors. Between two plasma shots, we can choose a new source point from any terminal by just entering the plasma co-ordinates. The positioning accuracy in the plasma is better than 1 mm. However, it should be noticed that the viewing cone is very narrow-angled (1.4°), as the diameter of the mirrors is small (10 cm) compared to the distance to the plasma (4 m). More details about mechanical construction, electronics and software can be found in [*Stei-94*].

3.1.5 Absorption spectroscopy

With some small changes, the NIS can also be used for absorption spectrometry (§2.3.2). Figure 3.4 suggest an experimental set-up.

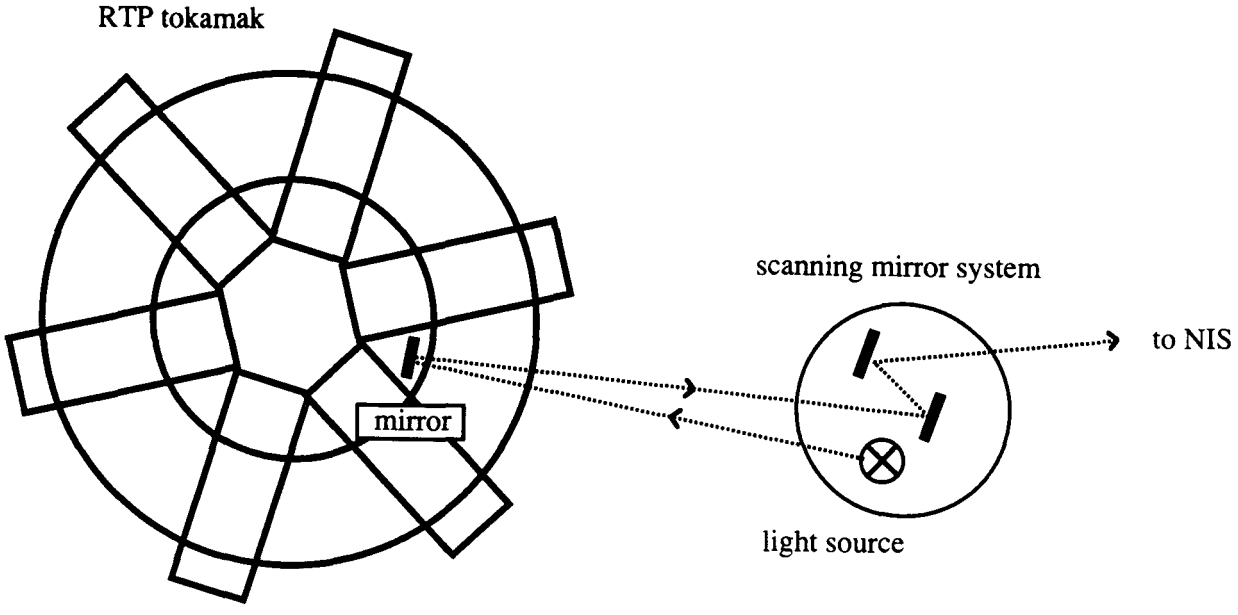

Figure 3.4 - Experimental set-up for absorption spectrometry with the NIS.

The light from a UV light source in the vacuum tank of the Scanning Mirror System (SMS) passes through the plasma. A concave mirror mounted at the high field side reflects the light back to the SMS. Another possibility is to mount the light source directly at the high field side. In the latter case it is easier to take still some advantage of the SMS. A light source that moves along or a wide-beam light source will be needed then. We can use continuum UV light sources like BRV (Ballofet, Romand, Vodar) sources or laser produced plasmas [*Mei2-87*]. It is also possible to use a laser as light source. Then we can do very selective measurements by tuning its frequency on a selected absorption line. It also allows a very high spatial resolution, but inversion techniques will be necessary as the measurements are line integrated now. There are several types of lasers available for the VUV region, like hydrogen, rare gas and fluoride lasers, (multiple) pumped anti-Stokes Raman lasers et cetera. A disadvantage is that most lasers are only tuneable over a very limited wavelength range, leaving many unobservable gaps in the range one wishes to cover.

3.2 Vacuum system

As mentioned before, the UV light in the lower part of the wavelength range covered by the NIS is absorbed by air. Therefore it is necessary that the whole system operates in high vacuum. Vacuum-technically, we can divide the system in three parts: the tokamak vessel, the scanning mirror system tank ("mirror tank") and the spectrometer tank. During a discharge, the mirror tank is in open connection with the tokamak. The mirror tank and the spectrometer tank are separated by the narrow (10 μm) entrance slit. As the slit has a very high resistance for gas flow, a large pressure difference (>10^4 mbar) can be achieved over it. We will only discus the vacuum system of the spectrometer tank here.

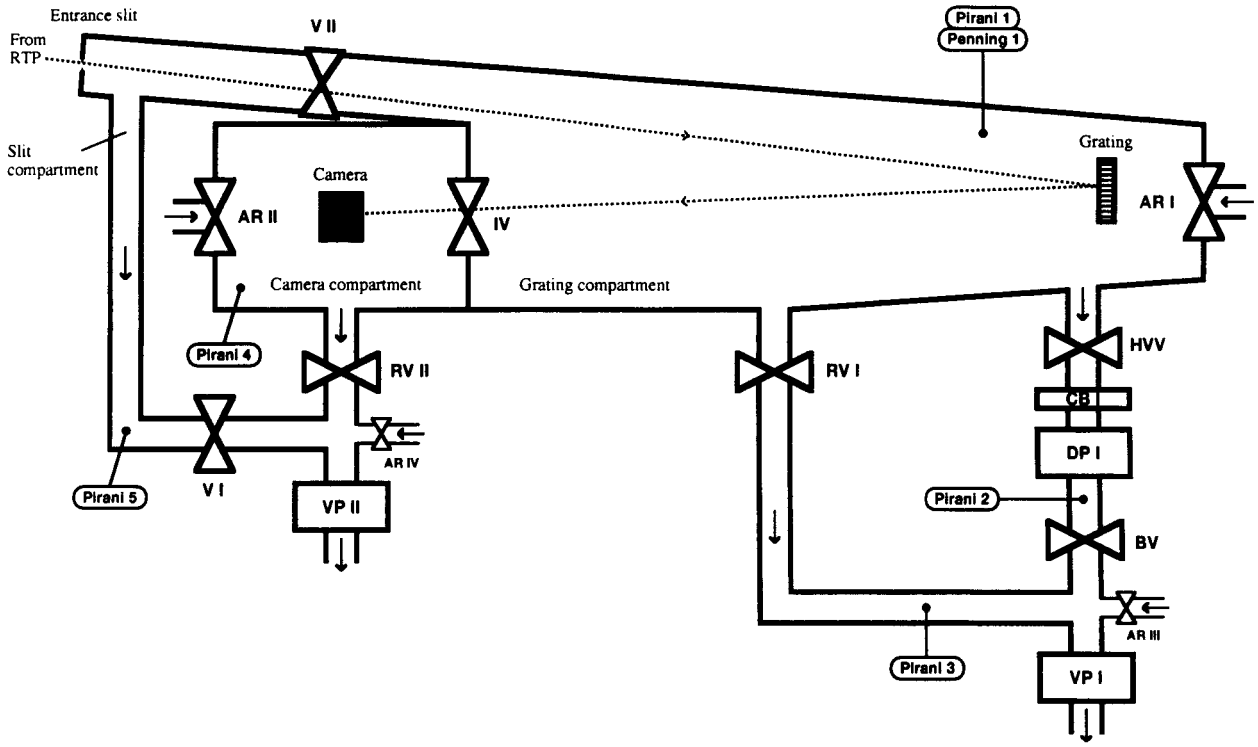

Figure 3.5 - Schematic view of the vacuum system of the spectrometer tank. The tank is divided in a grating, a camera and a slit compartment. Indicated are diffusion pump DP I; the rough vacuum pumps VP I and VP II; Chevron baffle CB I; high vacuum valve HVV, backing valve BV, roughing valves RV I and II, insulation valve IV, air release valves AR I - IV, and the valves V I and V II; and finally the several Pirani and Penning pressure meters. The dashed line gives the optical path.

The dimensions of the 1 cm thick steel vacuum tank are: length 7150 mm, diameter at camera end: 1020 mm, diameter at grating end: 600 mm.

Consider figure 3.5. Insulation valve IV divides the spectrometer tank into a grating compartment and a much smaller camera compartment. This valve allows to open the camera compartment, without breaking the vacuum in the other one. The part between V I and V II is called the slit compartment. In normal operation, only the valves HVV, BV, IV and V II are open. The five stage oil diffusion pump DP I (Edwards F1605, 3000 litres/sec with Chevron baffle) keeps all three compartments at high vacuum (~10^{-6} mbar), and is backed by two stage rotary pump VP I (Balzers Duo 170, 47 litres/sec). A diffusion pump is preferable to a turbomolecular pump because a large spectrometer like the NIS is very sensitive for vibrations, as they can cause resonance effects in the tank. For the same reason vibrations of the rough vacuum pumps are carefully damped. During the starting procedure, VP I pumps the grating compartment through roughing valve RV I down to rough vacuum. Two stage rotary pump V II (Precision PS 1000, 17 litres/sec) pumps the camera compartment via RV II. For the slit compartment, there is a free choice for pumping via V I or V II. Several Pirani and Penning manometers register the pressures at the indicated points. Table 3.4 gives the pump capacities and end pressures.

Table 3.4 - Overview of end pressures in situ and pump capacities. Types of pumps: DP I: Edwards F1605 five stage oil diffusion pump; VP I: Balzers Duo 170 two stage rotary pump; VP II: Precision PS 1000 two stage rotary pump.

Pump		Capacity [l/s]		End pressure [mbar]	Pressure meter
DP I	including baffle	3000	(at < 10^{-4} mbar)	$1 \cdot 10^{-6}$	Penning 1
VP I	as roughing pump	47	(at 1 atm)	$1 \cdot 10^{-1}$	Pirani 1
	as backing pump	44	(at 1 mbar)	$4 \cdot 10^{-2}$	Pirani 2
VP II		17	(at 1 atm)	$6 \cdot 10^{-2}$	Pirani 4

Figure 3.6 gives a measured pump-down curve for the grating compartment. We can distinguish three parts. After VP I has pumped down to 10^{-1} mbar in one and a half hour, the high vacuum valve HVV is opened gradually within about fifty minutes. The end pressure of 10^{-6} mbar is reached after three and a half hour.

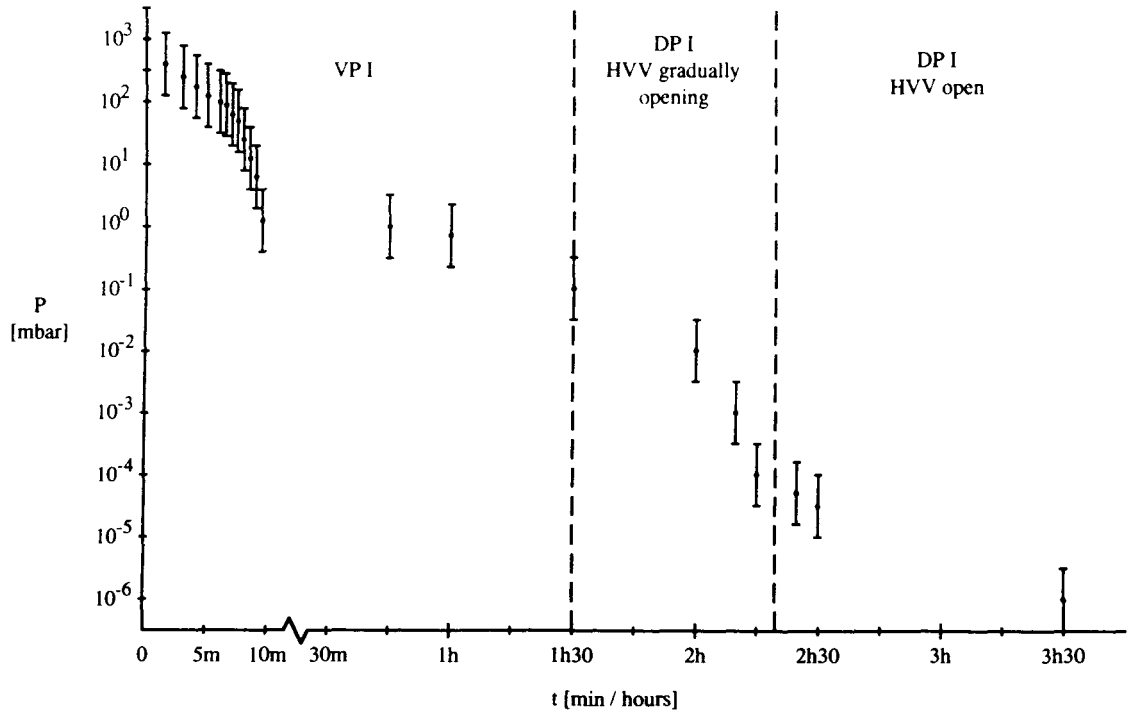

Figure 3.6 - Pump-down curve for the grating compartment. After VP I has pumped down to 10^{-1} mbar in one and a half hour, the high vacuum valve HVV is opened gradually within about fifty minutes. The end pressure of 10^{-6} mbar is reached after three and a half hour.

Vacuum control system

An electromechanical "dedicated computer" controls the continuously operating vacuum system. This half-automatically system controls all pumps and valves, and presents all information on a control panel. The manual control operations are intercepted and checked. It also checks the cooling systems, 3 phase power supplies, temperatures, pressures, et cetera. We choose for an electromechanical control system because of its reliability in the semiconductor unfriendly environment it has to operate: the tokamak plasma and the ECRH heating systems produce intense interfering fields. Although dedicated to its task the system is easy to adjust, due to its both electrical and mechanical modular construction. Appendix one gives the electrical schemes including a brief explanation.

The control system also prevents for damage to the optical system, by precluding oil from getting into the tank. The ultra violet light will decompose oil deposited on surface of the grating, leaving a carbon layer behind [*Hunt-79*]. Other arrangements to prevent oil from getting into the tank are the water cooled Chevron baffle CB I, which condenses oil vapour escaping from the diffusion pump, and the automatically air release valves AR III and AR IV.

3.3 Control and data acquisition

The normal incidence spectrometer is automated to a large extend. We can discriminate between control and data acquisition. As mentioned before, the positions of the grating, the camera and the mirrors, and the exposure time can be adjusted remotely between two plasma shots. A graphic user interface provides easy adjustment [*Os-95*].

Data reduction

The CCD camera produces 2.6 megabytes data each plasma shot. Position, intensity and shape of the spectral lines are determined automatically, also giving a considerable reducing of these large amounts of data [*Phil-90*]. The signals are first smoothened using a so-called spline noise filter. Lines are recognised by their negative intervals in the second derivative. Only lines that satisfy certain quality requirements are accepted. Photographic plates can also be measured automatically after digitising the data using an automatic comparator like the Zelacom.

Computer hardware

Figure 3.7 gives a schematic view of the hardware and bus configuration. The rectangular boxes indicate devices and the rounded boxes are interfaces. For storage and reduction of the rough data we use Athena, a Silicon Graphics Indigo work station (33 MHz MIPS R3000A processor). For each plasma shot, the reduced data are stored in a so-called DOM file on Zeus (Silicon Graphics Power Series 4D300, four R3000 processors). DOM (Data Organisation and Management) is the central data management system for all RTP diagnostics [*Donn-91*]. Any X-Terminal can be used as graphical user interface. All data transport and acquisition is done fully automatically, using Ethernet for the connections between the several devices.
The connection with the NIS is provided by the GPIB (General Purpose Interface Bus), which is connected to the Ethernet by an interface (see figure). The graphical user interface is running on Athena, but the positioning routines have to run on Helius, a Tatung Supercomp-station 10/30 (36 MHz Viking Superscalar SPARC Processor), as only this machine allows connection with the GPIB through ethernet. On a lower level, the CCD and the positioning electronics each have their own eight bits parallel Input/Output bus. The interfaces between the positioning electronics and the MPX (Multiple Purpose eXperimental) bus consist of dedicated electronics. The back-coupled positioning data is also stored in the DOM file. More details can be found in the literature [*Rijs-95*, *Stei-94*, *Stek-93*].

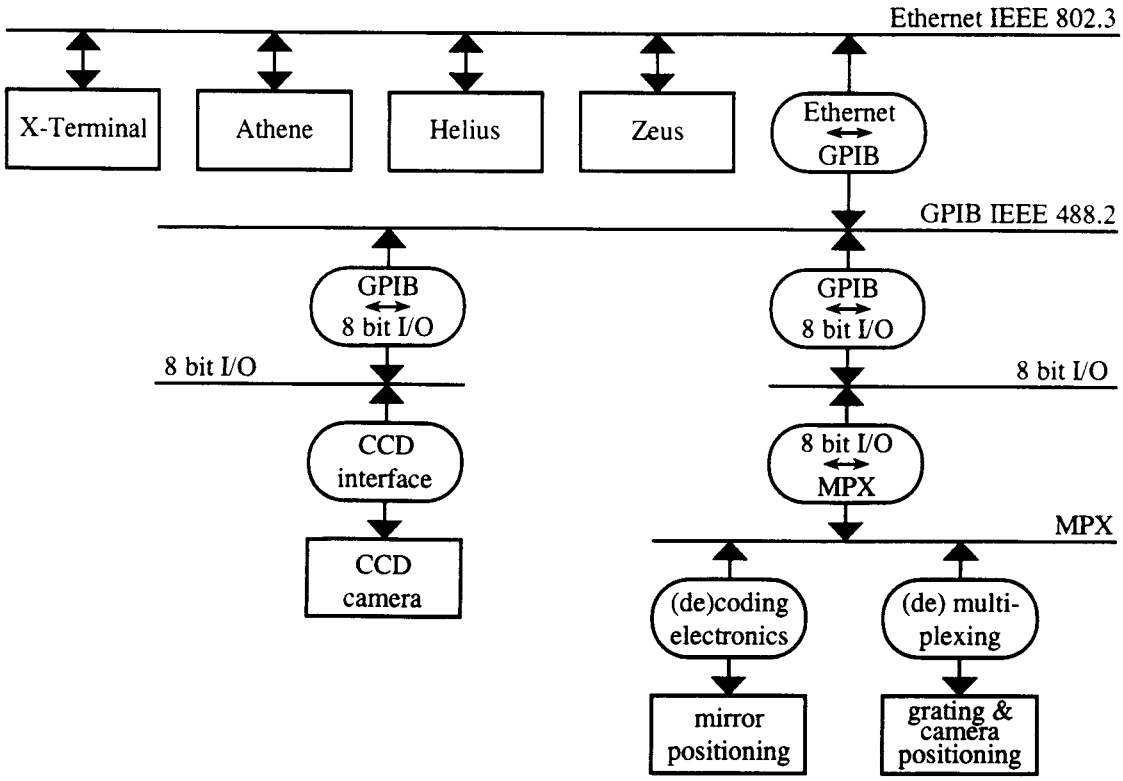

Figure 3.7 - Schematic view of the hardware configuration. The rectangular boxes indicate devices and the rounded boxes are interfaces. The CCD and the positioning electronics each have their own eight bits parallel Input/Output bus. The interfaces between the MPX (Multiple Purpose eXperimental) bus and the positioning electronics consist of dedicated electronics [Stei-94, Stek-93]. Other abbreviations: IEEE: Institute of Electronics and Electrical Engineers, GPIB: General Purpose Interface Bus.

3.4 Calibration and testing using neon and argon spectra

To provide a correct functioning of the spectrometer, the positions of camera, grating and slit have to be calibrated. In case of the NIS this means calibration of the positions of the actuators (§3.1). As the slit has a fixed position, we first positioned the grating such that the slit is on its focal curve. Using cross-wire calibration, we can keep the distance from grating to slit within 0.2 mm from the correct position, the limit where bending of light diffuses the spectral lines. The position of the camera has been calibrated photographically by just trying to get the spectral lines of a test light source as sharp as possible. We calculated a first estimation, taking the deviations of the Rowland circle for the used gratings into account. The results of the calibrations have been incorporated in the positioning software.

Pulsed hollow cathode discharge

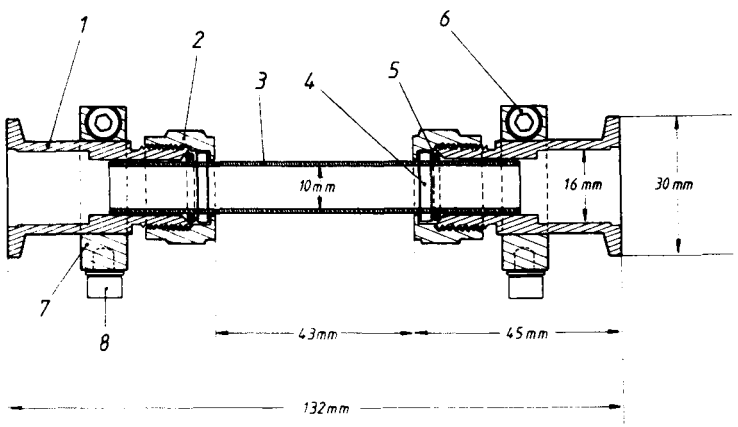

Figure 3.8 - Construction of the hollow cathode. 1 vacuum connecting flanges; 2 glass tube connecting rings; 3 glass tube; 4 synthetic ring; 5 O-ring; 6 clamping bolt; 7 terminal block; 8 electrode connecting bolt. Adapted from [Deet-86].

For calibration of the grating and camera positions, and for general testing, we used a neon pulsed hollow cathode discharge as light source. It gives a high yield of light and the spectral lines don't suffer any Stark broadening. Figure 3.8 gives the mechanical construction of the used hollow cathode [*Deet-86*, *Mei2-87*]. Because no imaging optics can be used, the light source has to be mounted directly before the slit to ensure a good distribution of the light over the grating surface. This has some disadvantages. Deposition of material clogs the slit, and electrical insulation of the slit from the vacuum tank is needed to suppress the tendency towards discharges between the aluminium electrodes and the slit [*Klee-64*]. The hollow cathode is

through a flow regulation valve connected to a neon source of constant pressure. The other end is, through the slit and valve V II (see figure 3.5), pumped by the diffusion pump. Rough vacuum pump VP II is not used and valve V I is closed. In this way an equilibrium pressure of 2 - 5 mbar is maintained in the hollow cathode, while the pressure in the spectrometer tank is 10^{-4} mbar. A higher neon pressure would lead to an inadmissible high pressure in the spectrometer tank, as the backing pump VP I cannot handle its gas flow.

Figure 3.9 gives the electrical scheme of the pulse generator used to supply the hollow cathode light source. It produces near rectangular shaped pulses with a current up to 2.5 kA and a repetition frequency adjustable between 0.1 and 6 Hz. As power switch we used a thyratron (a gas filled electron tube), as no semiconductors can handle the extremely high *dI/dt* occurring. An inductance-capacitor network is used for pulse shaping.

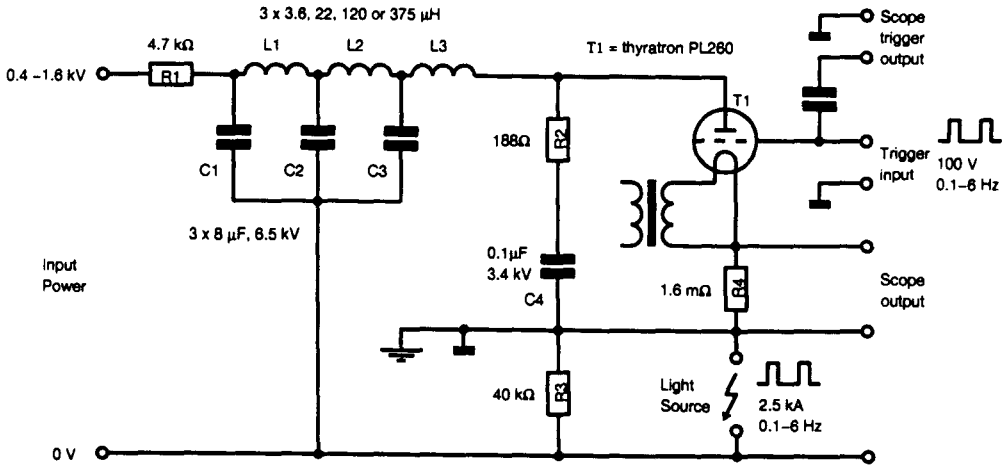

Figure 3.9 - The pulse generator used for the hollow cathode light source. It produces nearly rectangular shaped pulses with a current up to 2.5 kA and a repetition frequency adjustable between 0.1 and 6 Hz.
Thyratron T1 is used as power switch. It is triggered by an external pulse generator. The network consisting of C1 - C3 and L1 - L3 is used for pulse shaping. The voltage drop over R4 can be used as scope output. The other components are needed for a proper ignition of the thyratron. Notice the floating input power supply.

Figure 3.10 gives an example of a neon spectrum as measured with the NIS. The figure shows three different wavelength regions in the VUV. The spectrum has been taken photographically, using a pulsed hollow cathode discharge at three different peak currents, from 1350 to 2400 Amperes. We can recognise many Ne II and Ne III lines. The strong aluminium lines arise from the cathode material. We also find some carbon, nitrogen and oxygen lines, and the L_α line of hydrogen at 121.5670 nm The silicium lines are caused by the glass tube.

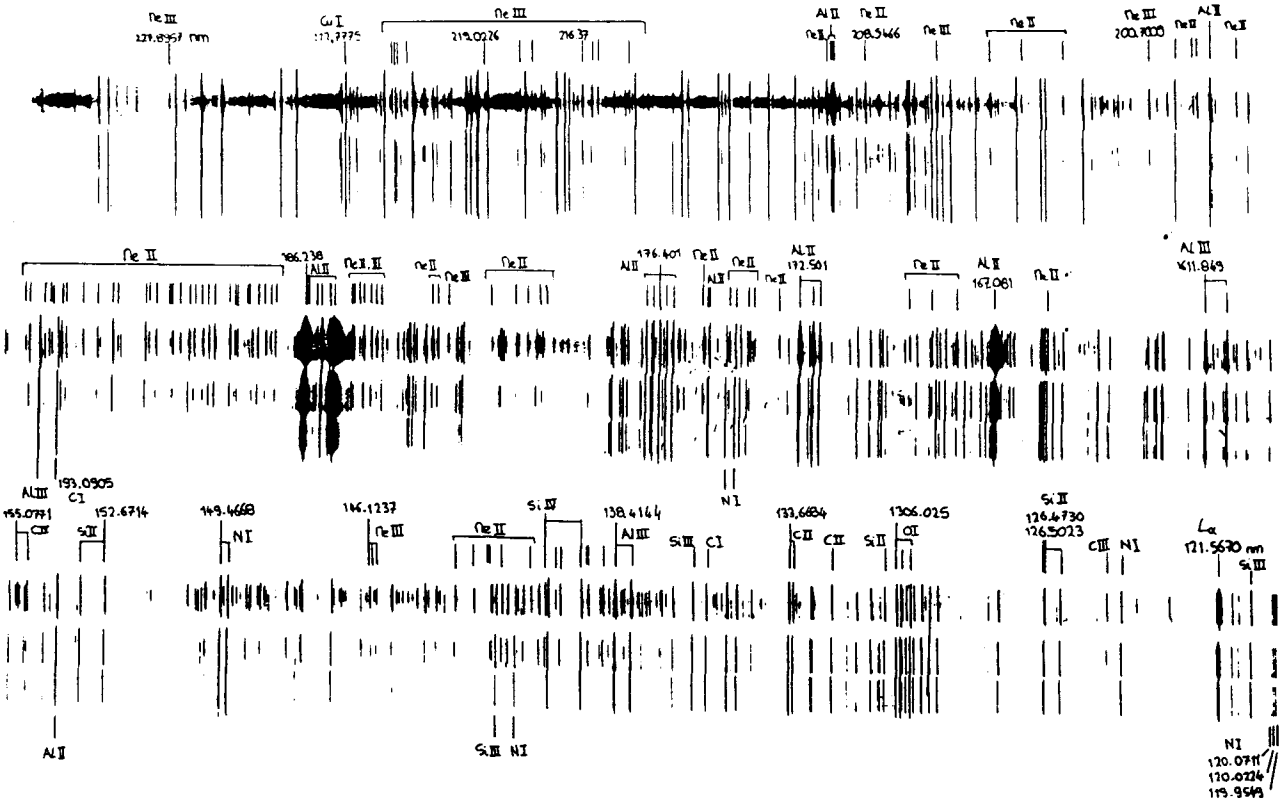

Figure 3.10 - Three wavelength regions of the neon spectrum in the VUV. The spectra have been taken photographically, using a pulsed hollow cathode discharge at three different peak currents: 2400 A (top row of each part of the spectrum), 1800 A (middle) and 1350 A (bottom). Several neon, aluminium, carbon, nitrogen, oxygen and silicium lines are indicated. All wavelengths are given in nanometers (1 nm = 10 Å). Unfortunately, this picture cannot show the many weak lines on the original photographic plates.

Argon spectra

First results of measurements on tokamak plasmas are not within the (time) range of this report, but will be published soon. To get yet an indication of the resolving power of the NIS, consider figure 3.11. It shows four wavelength regions of the argon spectrum in the VUV, each about 1 nm long. They have been taken photographically by the NIS as it was at the Zeeman laboratory [*Deet-86*]. As a light source, a gas injection discharge at four different peak currents from 2.5 kA till 22 kA, was used [*Mei2-87*]. Several Ar II till Ar VIII lines are indicated. As expected, higher currents give spectral lines of higher ionised argon ions, e.g. the Ar VIII line at 52 nm. The original photographic plate indicates a resolving power of 150,000.

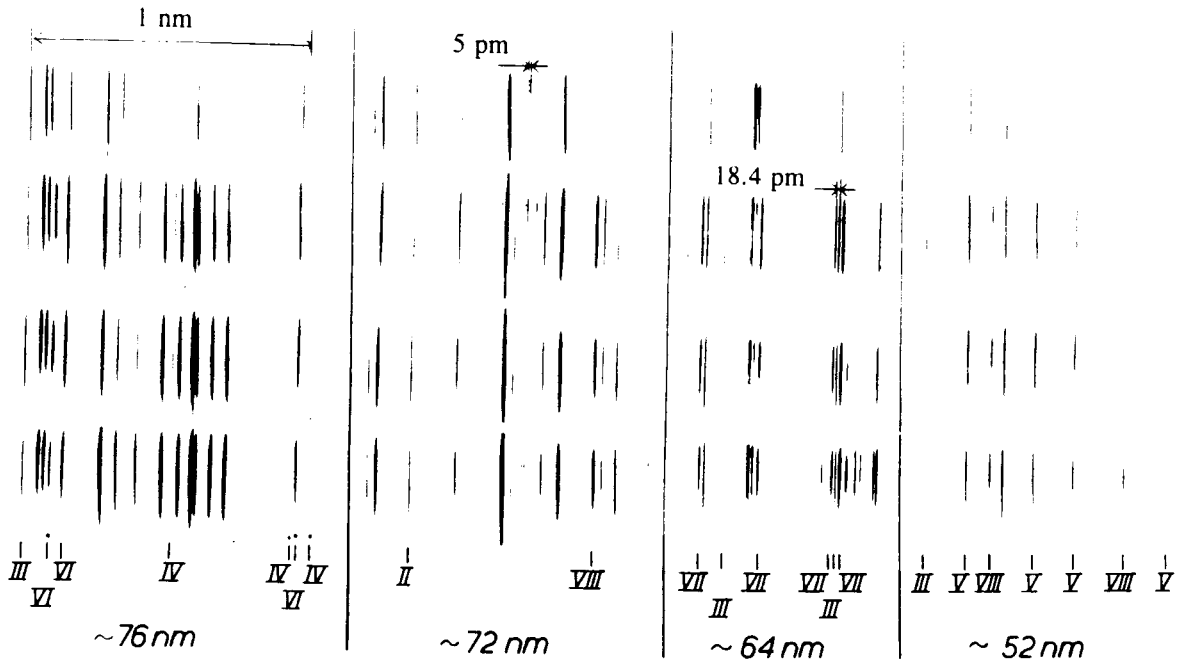

Figure 3.11 - Four wavelength regions of the argon spectrum in the VUV, each about 1 nm long. The spectra have been taken using a gas injection discharge, with four different peak currents, from 2.5 kA (top), 10, 16 to 22 kA (bottom). The original photographic plate indicates a resolving power of 150,000.

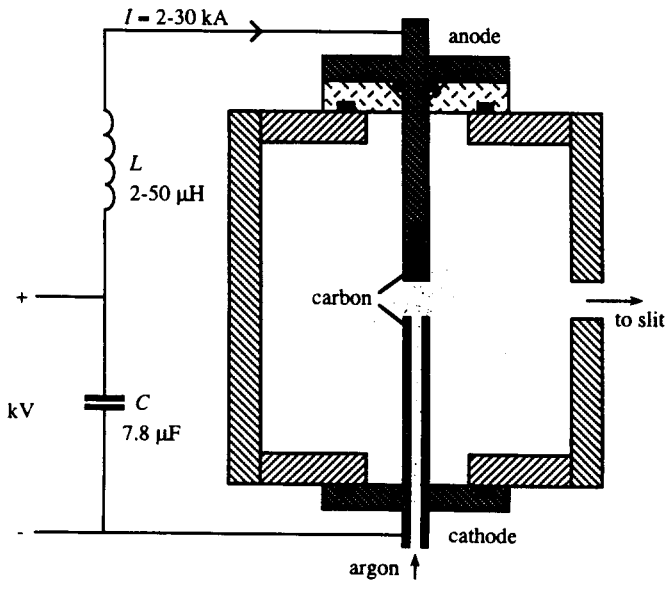

Figure 3.12 - Mechanical construction of the gas injection discharge light source. The source is triggered when a well-defined amount of argon is injected between the electrodes.

Figure 3.12 gives the mechanical construction of the gas injection discharge light source. It is specially designed for noble gas discharges. A high voltage is put over both electrodes in vacuum. A discharge is triggered by injecting a well-defined amount of gas, through the hollow cathode, between the electrodes. There is no thyratron necessary, as the source itself acts as a switch. The inductance-capacitor network is less complicate than the network used with the hollow cathode discharge (figure 3.9), but gives a poorer pulse shape. We planned to use the noble gas injection discharge again at the FOM Institute.

Scanning mirror system

All four actuators of the scanning mirror system (§3.1.4) have been tested, including the electronics and the graphical user interface. The vertical scan of the source point has also been calibrated. That means, the position of the actuator as a function of the vertical co-ordinate of the source point in the plasma (see appendix two) has been calibrated. The depth scan and the horizontal adjustment will follow soon. For the calibration we used a zirconium arc as light source. It gives a high yield of light concentrated in a small point. Just as for the camera and the grating, the results have been incorporated in the software.

Chapter 4

Conclusions and discussion

The main subject of RTP is to study transport processes. But in spite of the large number of diagnostics, the behaviour of impurities and plasma rotations could not be explored until recently. To meet this lack of information, the 6.65 m Normal Incidence Spectrometer was moved from the Amsterdam University. At the FOM Institute we successfully adapted it to measure the emission of radiation of the RTP tokamak plasmas (chapter three).

Some points of interest

The NIS opens an unexplored experimental area at RTP. At first we will perform photographic measurements to get an overview of the impurity species in the plasma. A photographic plate covers a large part of the accessible wavelength region at once.
A very interesting issue will be measuring the distribution of the several impurity ions using the Scanning Mirror System. We can compare the measured shells with the results calculated from the transport-corona model of paragraph 2.1.2 and determine the diffusion coefficient D and the convective flow velocity v. We have however to keep in mind that the SMS sees a cone-shaped part of the plasma. We will therefore probably have to correct the distribution measurements for this phenomenon.
In the core of the plasma the radial fluxes are small. Therefore we expect the steady state corona model to hold for the highly ionised metal impurities. Light impurities can only be measured at the plasma edge, where plasma parameters like n_e and T_e are often poorly known. To extrapolate the impurity densities to the centre of the plasma, we have to take the transport processes into account. Experiments should also give insight in the influence of all atomic processes mentioned in paragraph 2.1.2. Especially charge exchange processes are considered to be difficult to take into account.
The plasma rotation measurements can be compared with the results of the visible light spectrometer. The magnetic field measurements can be cross-checked against the values calculated from current density measurements. We could calculate the effective atomic charge Z_{eff} in principle from the measured impurity density profiles. The accuracy of the calculated Z_{eff} from impurity distributions is however limitted. For measuring the total power losses of a plasma, bolometric measurements are more useful than detailed spectral information. Difficulties in interpreting ion temperatures and electron temperatures and densities have already been discussed in chapter two so will not be repeated here.

The diagnostic power of the adapted NIS

The adapted NIS is a very powerful diagnostic: we can *measure a large number of quantities*, for instance impurity distributions, ion temperatures, plasma rotations and magnetic fields, as is theoretically founded in chapter two. In combination with the RIS (gRazing Incidence Spectrometer) which will become operational later this year, we can perform simultaneous measurements of poloidal and toroidal rotations at the same location in the plasma. The use of a CCD camera gives a *high temporal resolution* of 0.2 ms. This means that even fast phenomena like sawtooth oscillations (typical 1 ms) can be resolved. The Scanning Mirror System (SMS) allows two-dimensional scanning of the source point in the plasma, with a *spatial resolution* of about 1 cm. Two interchangeable gratings cover the accessible *wavelength region* of 35 - 400 nm, complementing the other spectrometers of the RTP spectroscopy programme (table 1.2). Its accessible wavelength region in combination with the SMS makes the NIS very suitable for doing core spectroscopy. The dimensions of the NIS and its grating properties make an extremely *high spectral resolving power* up to 400,000 possible. As the examples in paragraph 2.3 showed, fine structure and Zeeman components can easily be resolved. We can measure velocities down to 750 ms^{-1}, which is below the lowest expected plasma rotation velocities (> 10^3 ms^{-1}). Further, we can measure ion temperatures down to a few eV. This is more than adequate to measure edge plasma temperatures. The high resolving power makes the NIS also very suitable for absorption spectroscopy. Finally, the NIS is very *comfortable in use*: a graphical user interface provides fast and easy adjustment of the computer controlled optical system from any terminal, the data acquisition is computerised to a large extend and the vacuum system is controlled by an intelligent control system that automatically intervenes in case of any malfunction. It even intercepts and checks the manual control operations. As can be seen from this list, the NIS will be more than suitable to complete the lacking information mentioned before.

Test results

All actuators of the optical system (gratings, camera and SMS) have been tested, including the electronics and the graphical user interface. The positions of the gratings, the camera and the vertical scan of the SMS have also been calibrated. We implemented the calibration results into the software. We tested the CCD camera with the VIsible light Spectrometer (VIS). The neon and argon VUV spectra shown in paragraph 3.4 are taken photographically with the NIS. They indicate resolving powers up to 150,000 at 70 nm. The data reduction software decreases the amount of data more than 90 percent. The vacuum control system proves its value already for months.

Symbols and abbreviations

a	minor radius of the torus at the limiter	[m]
A_I	atomic mass number	[amu]
$A(p,q)$	transition probability for the transition from level p to level q	[s^{-1}]
b_1	image distance of scanning mirror 1	[m]
b_2	image distance of scanning mirror 2	[m]
B	magnetic field strength	[T]
B_ϕ	toroidal magnetic field	[T]
B_θ	poloidal magnetic field	[T]
c	velocity of light (= $2.99792458 \cdot 10^8$)	[ms^{-1}]
C	(position of) camera or photographic plate	[-]
cr	(subscript) collision and radiation term	[-]
d	groove distance	[m]
D	diffusion coefficient	[m^2s^{-1}]
e	electron charge (= $1.6021892 \cdot 10^{-19}$)	[C]
f	frequency of an emitted photon	[s^{-1}]
f_0	frequency emitted by a non moving ion	[s^{-1}]
f_1	focal length of scanning mirror 1	[m]
f_2	focal length of scanning mirror 2	[m]
f_I	fraction of impurity element I	[-]
$f(E)$	(Maxwellian) velocity distribution	[-]
$f(p,q)$	oscillator strength for the transition $p \rightarrow q$	[-]
F_1, F_1'	focal points of scanning mirror 1	[-]
F_2, F_2'	focal points of scanning mirror 2	[-]
g_L	Landé factor	[-]
$g(p)$	quantum statistical degeneration correction function for the level p	[-]
G	(position of) grating	[-]
h	Planck's constant (= $6.626176 \cdot 10^{-34}$)	[Js]
$\hbar$	Dirac's constant (= $1.054589 \cdot 10^{-34}$)	[Js]
I	impurity element	[-]
I_p	plasma current	[A]
j	quantum number for the total angular momentum of an electron	[-]
J	quantum number for total angular momentum of a system	[-]
k	Boltzmann's constant (= $1.380662 \cdot 10^{-23}$)	[JK^{-1}]
k	number of electrons in a subshell	[-]
$K(p,q)$	collision coefficient	[$m^{-3}s^{-1}$]

L	quantum number for total orbital angular momentum of a system	[-]
L_1	distance between entrance slit and scanning mirror 2 ($L_{1\,min}$...$L_{1\,max}$)	[m]
L_2	distance between both scanning mirrors ($L_{2\,min}$...$L_{2\,max}$)	[m]
L_3	distance between scanning mirror 1 and origin in plasma	[m]
m	spectral order of reflection (grating)	[-]
m_e	electron mass (= $9.109534 \cdot 10^{-31}$)	[kg]
m_i	ion mass	[kg]
m_I	impurity ion mass	[kg]
m_J	magnetic quantum number for z-component of J	[kg]
n	total plasma density	[m^{-3}]
$n(p)$	density of excited level p	[m^{-3}]
n_e	electron density	[m^{-3}]
n_i	ion density	[m^{-3}]
n_I	impurity ion density	[m^{-3}]
n_H	density of neutral hydrogen atoms	[m^{-3}]
$n(Z)$	density of atomic or ionic ground level	[m^{-3}]
$n(p)$	density of atomic or ionic excited level p (of ionisation stage Z)	[m^{-3}]
$n(Z+1)$	density of the ground level of the next higher ionisation stage	[m^{-3}]
N	number of grooves of a grating	[-]
P	point at grating	[-]
P	source point in the plasma (in appendix 2)	[-]
$P_{Br(DT)}$	bremsstrahlung power (DT reaction)	[Wm^{-3}]
r	radial co-ordinate	[m]
r_{pq}	matrix element of the dipole oscillator for the transition $p \rightarrow q$	[-]
R	radius of curvature of concave spherical grating = diameter Rowland circle	[m]
R	distance to the axis of the torus	[m]
R_0	major radius of the torus	[m]
$\mathfrak{R}$	(total) resolving power	[-]
$\mathfrak{R}_c$	resolving power of the camera or photographic plate	[-]
$\mathfrak{R}_g$	resolving power of the grating	[-]
$\mathfrak{R}_s$	resolving power of the slit	[-]
t	time	[s]
S	(position of) entrance slit	[-]
S	quantum number for total spin of a system	[-]
T , $\hat{T}$	temperature	[K, keV]
T_e, $\hat{T}_e$	electron temperature	[K, keV]
T_i, $\hat{T}_i$	ion temperature	[K, keV]
T_I, $\hat{T}_I$	impurity ion temperature	[K, keV]

v	velocity	[ms^{-1}]
v_0	convective flow velocity at the plasma edge	[ms^{-1}]
v_1	object distance of scanning mirror 1	[m]
v_2	object distance of scanning mirror 2	[m]
v_e	electron velocity	[ms^{-1}]
V_{loop}	loop voltage driving plasma current	[V]
W	(effective) width of grating	[m]
x	plasma co-ordinate tangent to toroidal axis	[m]
y	plasma co-ordinate in radial direction	[m]
z	plasma co-ordinate in vertical direction	[m]
Z_{eff}	effective atomic charge	[amu]
Z_I	charge of impurity element I	[-]
α	angle of incidence (grating)	[rad]
β	angle of reflection (grating)	[rad]
γ_1	turning angle of scanning mirror 1 around vertical axis	[rad]
γ_2	turning angle of scanning mirror 2 around vertical axis	[rad]
$\Gamma(Z)$	radial flux of atoms or ions in ground level	[m^{-2}s^{-1}]
$\Gamma(p)$	radial flux of atoms or ions in excited level p	[m^{-2}s^{-1}]
$\Gamma(Z+1)$	radial flux of ions in the ground level of the next higher ionisation stage	[m^{-2}s^{-1}]
δ_1	tilting angle of scanning mirror 1 around horizontal axis	[rad]
$\Delta E(p,q)$	energy difference between the levels p and q	[J, eV]
Δf	Doppler frequency shift	[ms^{-1}]
Δs	spatial resolution of camera or photographic plate	[-]
$\Delta\lambda$	(resolvable) wavelength difference	[m]
$\Delta\lambda_c$	smallest resolvable wavelength difference by the camera	[m]
$\Delta\lambda_g$	smallest resolvable wavelength difference by the grating	[m]
$\Delta\lambda_s$	smallest resolvable wavelength difference by the slit	[m]
ε_0	permittivity of vacuum (= 8.85415·10^{-12})	[Fm^{-1}]
λ	wavelength	[m]
Λ	escape factor (correction coefficient for reabsorbing of radiation)	[-]
μ_B	Bohr magneton (= 9.274078·10^{-24})	[Jm^{2}T^{-1}]
θ	(of moving ion) angle to line of sight of observer	[rad]
$\rho(f,T)$	(emitted) energy density	[Jm^{-3}s]
τ_E	energy confinement time	[s]
σ	wave number	[m^{-1}]
$\sigma(p,q)$	cross-section for the collisional transition from p to q	[m^2]
σ^{cx}	cross-section for charge exchange	[m^2]

Abbreviations

CCD	Charge Coupled Device
cr	Collision Radiation (term)
DOM	Data Organisation and Management
FOM	Stichting voor Fundamenteel Onderzoek der Materie
GPIB	General Purpose Interface Bus.
IEEE	Institute of Electronics and Electrical Engineers
MCP	MultiChannel Plate
MLM	MultiLayer Mirror
MPX	Multiple Purpose eXperimental (bus)
NIS	Normal Incidence Spectrometer
QSS	Quasi Steady State (approximation)
RIS	gRazing Incidence Spectrometer
RTP	Rijnhuizen Tokamak Project
SMS	Scanning Mirror System
VIS	VIsible light Spectrometer
VUV	Vacuum Ultra Violet

Abbreviations concerning the vacuum system are explained in figure A3.1.

References

[*Behr-85*] K.H. Behringer et al, *Impurity and radiation studies during the JET ohmic heating phase*, JET report P(85)08, 1985.

[*Behr-86*] K. Behringer, *Spectroscopic Diagnostics on JET*, JET report P(86)10, 1986.

[*Beut-45*] H.G. Beutler, *The theory of the concave grating*, Journ. Opt. Soc. Am. **35**, 311-350, 1945.

[*Boge-93*] P. Bogen, *Spectroscopic diagnostics of edge plasmas in tokamaks*, Phys. Scr. **T47**, 102-109, 1993.

[*Chen-74*] F.F. Chen, *Introduction to plasma physics*, Plenium Press, New York, London, 1974.

[*Deet-86*] A.J. Deetman, *Vacuum technology, vacuum spectroscopy and pulsed licht sources*, Zeeman Laboratorium, 1986.

[*Donn-91*] A.J.H. Donné et al., *Rijnhuizen report 91-207*, 1991.

[*Hech-87*] E. Hecht, *Optics* , Addison-Wesley, Reading Massachusetts, 1987.

[*Hell-94*] M. von Hellermann, *Quantitative Spectroscopy for fusion plasmas*, JET report P(94)08, 1994.

[*Hey-94*] J.D. Hey, Y.T. Lie, D. Rusbüldt and E. Hintz, *Doppler broadening and magnetic field effects on some ion impurity spectra emitted in the boundary layer of a tokamak plasma*, Plasma Phys. **34**, 725-747, 1994.

[*Hunt-79*] W.R. Hunter and D.W. Angel, *Effect of diffusion pump oil contamination on diffraction grating efficiency in the VUV spectral region*, Appl. Opt. **18**, 3506-3509, 1979.

[*Hutc-90*] I.H. Hutchinson, *Principles of plasma diagnostics*, Cambridge University Press, Cambridge, 1990.

[*Isle-84*] R.C. Isler, *Impurities in tokamaks*, Nuclear Fusion **24**, 1599-1678, 1984.

[*Klee-64*] Th.A.M. van Kleef and J.F. Schröder, *A 6.650 m vacuum spectrograph*, Appl. Sci. Res. **B 11**, 465-478, 1964.

[*Koni-94*] J.A. Konings, *Electron thermal transport in tokamak plasmas*, thesis, Utrecht, 1994.

[*Lack-82*] K. Lackner, K. Behringer, W. Engelhardt and R. Wunderlich, Z. Naturforsch. **37a**, 931-938, 1982.

[*Long-73*] R.S. Longhurst, *Geometrical and physical optics*, Longman, New York, 1973

[*Lotz-68*] W. Lotz, *Subshell binding energies of atoms and ions from hydrogen to zinc*, Journ. Opt. Soc. Am. **58**, 915-921, 1968.

[*Meij*] F.G. Meijer, private communication.

[*Meij-79*] F.G. Meijer, *Construction, adjustment and performance of a 6.600 m grazing incidence vacuum spectrograph*, Journ. Phys. E **12**, 129-135, 1979.

[*Meij-87*] F.G. Meijer, *The use of gratings in the vacuum ultraviolet*, Opt. Appl. **17**, 255-264, 1987.

[*Mei2-87*] F.G. Meijer, *Lightsources: ionisation and excitation of atoms*, Opt. Appl. **17**, 237-254, 1987.

[*Mort-91*] D.C. Morton, *Atomic data for reconance absorbtion lines. I. Wavelengths longward of the Lyman limit*, Astrophys. Journ. **77**, Suppl., 119-202, 1991.

[*Orns-93*] L.Th.M. Ornstein, *Energy resources; The Safety of fusion reactors*, First Carolus Magnus summer school on plasma physics, Vaals 6-17 Sept. 1993.

[*Os-95*] P. van den Os, *Besturing van de NIS* **2-3**, FOM Rijnhuizen, 1995.

[*Phil-90*] P.H.T. Philipsen, *Automatische meting van spectraallijnen*, Zeeman Laboratorium, 1990.

[*Rijs-95*] J. van Rijswijk, *Software for the NIS* **1-3**, FOM Rijnhuizen, 1994-1995.

[*Sai-68*] T. Sai et al, *On Beutler's theory of the concave grating*, Sci. light **17**, 11-24, 1968.

[*Sho-68*] B.W. Shore and D.H. Menzel, *Principles of atomic spectra*, John Wiley and Sons, New York, 1968.

[*Sijd-92*] B. van der Sijde, *Inleiding plasmafysica*, dictaat nr. 3461 bij het gelijknamige college, Technische Universiteit Eindhoven, 1992.

[*Stei-94*] H.C.J. Steinmeijer, *De besturing van het scan-spiegelsysteem voor de Normale Inval Spectrograaf*, FOM Rijnhuizen, 1994.

[*Stek-93*] A. Stek, *De besturing van de instelling van het tralie en de CCD-camera in de 6.65m normale inval spectrometer*, FOM Rijnhuizen, 1993.

[*Stri-66*] A.R. Striganov, N.S. Sventitschkii, *Tabli spektral linii neutral i ionizovann atomov*, Atomgzdat Moskva, 1966.

[*Wess-87*] J. Wesson, *Tokamaks*, Clarendon Press, Oxford, 1987.

[*Zaid-70*] A.N. Zaidel, V.K. Prokof'ef, S.M. Raiskii, V.A. Slavnyi and E.Ya. Shreider, *Tables of spectral lines*, IFI/Plenium, New York - London, 1970.

[*Zast-91*] K.D. Zastrow, J.H. Brzozowski, E. Källne and H.P. Summers, *Spectroscopic measurement of electron temperature and electron density at the Extrap-T1 experiment*, TRITRA-PFU-91-09 report, 1991.

Appendices

Appendix 1

Spectral lines in the VUV

The tables in this appendix give the strongest spectral lines of several ionisation states of the elements hydrogen, boron, carbon, oxygen, iron and nickel, in the region 35 nm - 400 nm. Multiplets are not always completely listed.

Table A1.1 - Strong lines of Hydrogen ($Z_H = 1$) in the region 35 nm - 400 nm [Mort-91, Stri-66]

Ion Configuration (ionisation energy [eV])	*Wavelength [nm]*	*Energy lower level [eV]*	*Energy upper level [eV]*	*Transition lower level - upper level (notation: $nl^{2S+1}L_J$)*
H I *$1s^1\ ^2S_{1/2}$ (13.5984)*	*121.5670*	*0.00*	*10.20*	*$1s\ ^2S_{1/2}$ - $2p\ ^2P$*
	102.5722	*0.00*	*12.09*	*$1s\ ^2S_{1/2}$ - $3p\ ^2P$*
	97.2537	*0.00*	*12.75*	*$1s\ ^2S_{1/2}$ - $4p\ ^2P$*
	94.9743	*0.00*	*13.06*	*$1s\ ^2S_{1/2}$ - $5p\ ^2P_{3/2,\ 1/2}$*

Table A1.2 - Strong lines of several ionisation states of Boron (Z_B = 5) in the region 35 nm - 400 nm [Mort-91, Zaid-70]. The non-italic printed lines are referred to in the text.

Ion Configuration (ionisation energy [eV])	*Wavelength [nm]*	*Energy lower level [eV]*	*Energy upper level [eV]*	*Transition lower level - upper level (notation: $nl^{k\ 2S+1}L_J$)*
B I *$1s^2\ 2s^2\ 2p^1$ (8.2980)*	*249.74058*	*0.00*	*4.96*	*$2p\ ^2P$ - $3s\ ^2S_{1/2}$*
	249.77231	*0.00*	*4.96*	*$2p\ ^2P$ - $3s\ ^2S_{1/2}$*
	249.67715	*0.00*	*4.96*	*$2p\ ^2P$ - $3s\ ^2S_{1/2}$*
	182.62317	*0.00*	*6.79*	*$2p\ ^2P$ - $3d\ ^2D$*
	182.64047	*0.00*	*6.79*	*$2p\ ^2P$ - $3d\ ^2D$*
	182.63990	*0.00*	*6.79*	*$2p\ ^2P$ - $3d\ ^2D$*
	182.58960	*0.00*	*6.79*	*$2p\ ^2P$ - $3d\ ^2D$*
	137.8921	0.00	8.99	$2p\ ^2P$ - $2p^2\ ^2P$
	137.9165	0.00	8.99	$2p\ ^2P$ - $2p^2\ ^2P$
	137.8944	0.00	8.99	$2p\ ^2P$ - $2p^2\ ^2P$
	137.8875	0.00	8.99	$2p\ ^2P$ - $2p^2\ ^2P$
	137.8654	0.00	8.99	$2p\ ^2P$ - $2p^2\ ^2P$
B II *$1s^2\ 2s^2$ (25.149)*	*136.2461*	*0.00*	*9.09*	*$2s^2\ ^1S_0$ - $2p\ ^1P_1$*
B III *$1s^2\ 2s$ (37.920)*	*206.723*	*0.00*	*6.00*	
	206.577	*0.00*	*6.00*	

Table A1.3 - Strong lines of several ionisation states of Carbon (Z_C = 6) in the region 35 nm - 400 nm [Mort-91, Stri-66]. The non-italic printed lines are referred to in the text.

Ion Configuration (ionisation energy [eV])	*Wavelength [nm]*	*Energy lower level [eV]*	*Energy upper level [eV]*	*Transition lower level - upper level (notation: $nl^k\ ^{2S+1}L_J$)*
C I *$1s^2\ 2s^2\ 2p^2\ ^3P_0$ (11.2603)*	*156.140*	*0.00*	*7.95*	*$2p^2\ ^3P_2$ - $2p^3\ ^3D_3$*
	156.0702	*0.00*	*7.95*	*$2p^2\ ^3P_1$ - $2p^3\ ^3D_{2,1}$*
	143.2115	*4.18*	*12.84*	*$2p^3\ ^5S_2$ - $3s\ ^5P_2$*
	143.1595	*4.18*	*12.84*	*$2p^3\ ^5S_2$ - $3s\ ^5P_3$*
C II *$1s^2\ 2s^2\ 2p^1\ ^2P_{1/2}$ (24.381)*	392.0693	16.33	19.49	$3p\ ^2P_{3/2}$ - $4s\ ^2S_{1/2}$
	391.8978	16.33	19.49	$3p\ ^2P_{1/2}$ - $4s\ ^2S_{1/2}$
	133.5684	*0.01*	*9.29*	*$2p\ ^2P_{3/2}$ - $2p^2\ ^2D_{5/2}$*
	133.4515	*0.00*	*9.29*	*$2p\ ^2P_{1/2}$ - $2p^2\ ^2D_{3/2}$*
	103.7017	*0.01*	*11.96*	*$2p^2\ P_{3/2}$ - $2p^2\ ^2S_{1/2}$*
	103.6330	*0.00*	*11.96*	*$2p\ ^2P_{1/2}$ - $2p^2\ ^2S_{1/2}$*
	90.4468	*0.01*	*13.71*	*$2p\ ^2P_{3/2}$ - $2p^2\ ^2P_{1/2}$*
	90.4134	*0.01*	*13.72*	*$2p\ ^2P_{3/2}$ - $2p^2\ ^2P_{3/2}$*
	90.3950	*0.00*	*13.71*	*$2p\ ^2P_{1/2}$ - $2p^2\ ^2P_{1/2}$*
	90.3609	*0.00*	*13.72*	*$2p\ ^2P_{1/2}$ - $2p^2\ ^2P_{3/2}$*
	687355	*0.01*	*18.05*	*$2p\ ^2P_{3/2}$ - $3d\ ^2D_{5/2}$*
	687059	*0.00*	*18.04*	*$2p\ ^2P_{1/2}$ - $3d\ ^2D_{3/2}$*
C III *$1s^2\ 2s^2\ ^1S_0$ (47.881)*	97.7026	0.00	12.69	$2s^2\ ^1S_0$ - $2p\ ^1P_1$
	45.9633	*6.49*	*33.47*	*$2p\ ^3P_2$ - $3d\ ^3D_1$*
C IV *$1s^2\ 2s^1\ ^2S_{1/2}$ (64.490)*	*155.0771*	*0.00*	*7.99*	*$2s\ ^2S_{1/2}$ - $2p\ ^2P_{1/2}$*
	154.8185	*0.00*	*8.01*	*$2s\ ^2S_{1/2}$ - $2p\ ^2P_{3/2}$*
	38.4178	*8.01*	*40.28*	*$2p\ ^2P_{3/2}$ - $3d\ ^2D_{5/2}$*
	38.4032	*7.99*	*40.28*	*$2p\ ^2P_{1/2}$ - $3d\ ^2D_{3/2}$*

Table A1.4 - Strong lines of several ionisation states of Oxygen (Z_O = 8), in the region 35 nm - 400 nm [Mort-91, Stri-66, Zast-91].

Ion Configuration (ionisation energy [eV])	*Wavelength [nm]*	*Energy lower level [eV]*	*Energy upper level [eV]*	*Transition lower level - upper level (notation: $nl^{k\ 2S+1}L_J$)*
O I $1s^2\ 2s^2\ 2p^4\ ^3P_2$ (13.6181)	130.6025	0.03	9.52	$2p^4\ ^3P_0$ - $3s\ ^3S_1$
	130.4866	0.02	9.52	$2p^4\ ^3P_1$ - $3s\ ^3S_1$
	130.2173	0.00	9.52	$2p^4\ ^3P_2$ - $3s\ ^3S_1$
	104.0941	0.02	11.93	$2p^4\ ^3P_1$ - $4s\ ^3S_1$
	103.9233	0.00	11.93	$2p^4\ ^3P_2$ - $3s\ ^3S_1$
	102.7433	0.02	12.09	$2p^4\ ^3P_1$ - $3d^3\ D_{2,\ 1}$
	98.8776	0.00	12.54	$2p^4\ ^3P_2$ - $3s'\ ^3D_3$
O II $1s^2\ 2s^2\ 2p^3\ ^4S_{3/2}$ (35.146)	91.978	-	-	-
	83.4462	0.00	14.86	$2p^3\ ^4S_{3/2}$ - $2p^4\ ^4P_{5/2}$
	83.3326	0.00	14.88	$2p^3\ ^4S_{3/2}$ - $2p^4\ ^4P_{3/2}$
	71.8562	3.33	20.58	$2p^3\ ^2D_{3/2}$ - $2p^4\ ^2D_{3/2,\ 5/2}$
	71.8484	3.32	20.58	$2p^3\ ^2D_{5/2}$ - $2p^4\ ^2D_{3/2,\ 5/2}$
O III $1s^2\ 2s^2\ 2p^2\ ^3P_0$ (54.934)	83.5292	0.04	14.88	$2p^2\ ^3P_2$ - $2p^3\ ^3D_3$
	83.3742	0.01	14.88	$2p^2\ ^3P_1$ - $2p^3\ ^3D_{1,\ 2}$
	70.3850	0.04	17.65	$2p^2\ ^3P_2$ - $2p^3\ ^3P_{1,\ 2}$
	70.2899	0.01	17.65	$2p^2\ ^3P_1$ - $2p^3\ ^3P_{1,\ 2}$
	70.2822	0.01	17.65	$2p^2\ ^3P_1$ - $2p^3\ ^3P_0$
	70.2332	0.00	17.65	$2p^2\ ^3P_0$ - $2p^3\ ^3P_1$
	59.9598	2.51	23.19	$2p^2\ ^3D_2$ - $2p^3\ ^1D_2$
	59.7818	5.35	26.09	$2p^2\ ^3S_0$ - $2p^3\ ^1P_1$
	52.5795	2.51	26.09	$2p^2\ ^1D_2$ - $2p^3\ ^1P_1$
	50.8182	0.01	24.43	$2p^2\ ^3P_2$ - $2p^3\ ^3S_1$
	50.7683	0.01	24.43	$2p^2\ ^3P_1$ - $2p^3\ ^3S_1$
	50.7391	0.00	24.43	$2p^2\ ^3P_0$ - $2p^3\ ^3S_1$

Table A1.4 - Strong lines of several ionisation states of Oxygen (continued)

Ion Configuration (ionisation energy [eV])	*Wavelength [nm]*	*Energy lower level [eV]*	*Energy upper level [eV]*	*Transition lower level - upper level (notation: $nl^{k\ 2S+1}L_J$)*
O IV $1s^2\ 2s^2\ 2p^1\ ^2P_{1/2}$ *(77.394)*	*78.7710*	*0.00*	*15.74*	$2p\ ^2P_{1/2} - 2p^2\ ^2D_{3/2}$
	55.5262	*0.05*	*22.38*	$2p\ ^2P_{3/2} - 2p^2\ ^2P_{1/2}$
	55.4514	*0.00*	*22.41*	$2p\ ^2P_{3/2} - 2p^2\ ^2P_{3/2}$
	55.4074	*0.00*	*22.38*	$2p\ ^2P_{1/2} - 2p^2\ ^2P_{1/2}$
	55.3328	*0.00*	*22.41*	$2p\ ^2P_{1/2} - 2p^2\ ^2P_{3/2}$
O V $1s^2\ 2s^2\ ^1S_0$ *(113.873)*	*62.9732*	*0.00*	*19.69*	$2s^2\ ^1S_0 - 2p\ ^1P_1$
O VI $1s^2\ 2s\ ^2S_{1/2}$ *(138.080)*	*103.1912*	*0.00*	*12.01*	$2s\ ^2S_{1/2} - 2p\ ^2P_{3/2}$

Table A1.5 - Some strong lines of neutral Iron (Z_{Fe} = 26), in the region 35 nm - 400 nm [Mort-91, Stri-66]. The letters are used for alphabetical numbering of the levels: a, b, c,... for the upper level and z, y, x,... for the lower level.

Ion Configuration (ionisation energy [eV])	*Wavelength [nm]*	*Energy lower level [eV]*	*Energy upper level [eV]*	*Transition lower level - upper level (notation: $^{2S+1}L_J$)*
Fe I $1s^2\ 2s^2\ 2p^6\ 3s^2\ 3p^6\ 3d^6\ 4s^2\ ^5D_4$ *(7.9024)*	*385.99132*	*0.00*	*3.21*	$a\ ^5D_4 - z\ ^5D_4$
	382.58834	*0.91*	*4.16*	$a\ ^5F_4 - y\ ^5D_3$
	382.04274	*0.86*	*4.11*	$a\ ^5F_5 - y\ ^5D_4$
	374.94875	*0.91*	*4.22*	$a\ ^5F_4 - y\ ^5F_4$
	373.48659	*0.86*	*4.18*	$a\ ^5F_5 - y\ ^5F_5$
	371.99367	*0.00*	*3.33*	$a\ ^5D_4 - z\ ^5F_5$
	358.1195	*0.86*	*4.32*	$a\ ^5F_5 - z\ ^5G_6$
	302.06405	*0.00*	*4.11*	$a\ ^5D_4 - y\ ^5D_4$

Table A1.6 - Some strong lines of neutral Nickel (Z_{Ni} = 28) in the region 35 nm - 400 nm [Mort-91]

Ion Configuration (ionisation energy [eV])	*Wavelength [nm]*	*Energy lower level [eV]*	*Energy upper level [eV]*	*Transition lower level - upper level (notation: $nl^{k\ 2S+1}L_J$)*
Ni I *$1s^2\ 2s^2\ 2p^6\ 3s^2\ 3p^6\ 3d^8\ 4s^2$ (7.6398)*	*337.0531*			$4s^2\ ^3F$ -
	234.6259			$4s^2\ ^3F$ - ^3D
	232.0744			$4s^2\ ^3F$ - ^3G
	231.1669			$4s^2\ ^3F$ - ^3F
	229.0690			$4s^2\ ^3F$ -

Appendix 2

Scanning mirror system

The scanning mirror system described in chapter three provides two-dimensional scanning of the source point through the plasma. This appendix gives the formulas that relate a certain position in the plasma to the mirror positions.

The scanning mirror system covers a toroidal section of the plasma. For our calculations, we define a Cartesian co-ordinate system (figure A2.1), neglecting the toroidal symmetry. The "depth co-ordinate" y is defined equal to the radial co-ordinate r. The horizontal x-co-ordinate is defined tangent to the toroidal axis, and the z-co-ordinate is the vertical co-ordinate. To simplify the calculations we take in first instance L_1 parallel to the y-axis in figure A2.1. It can easy be "turned back" to its real position afterwards, without violating the results.

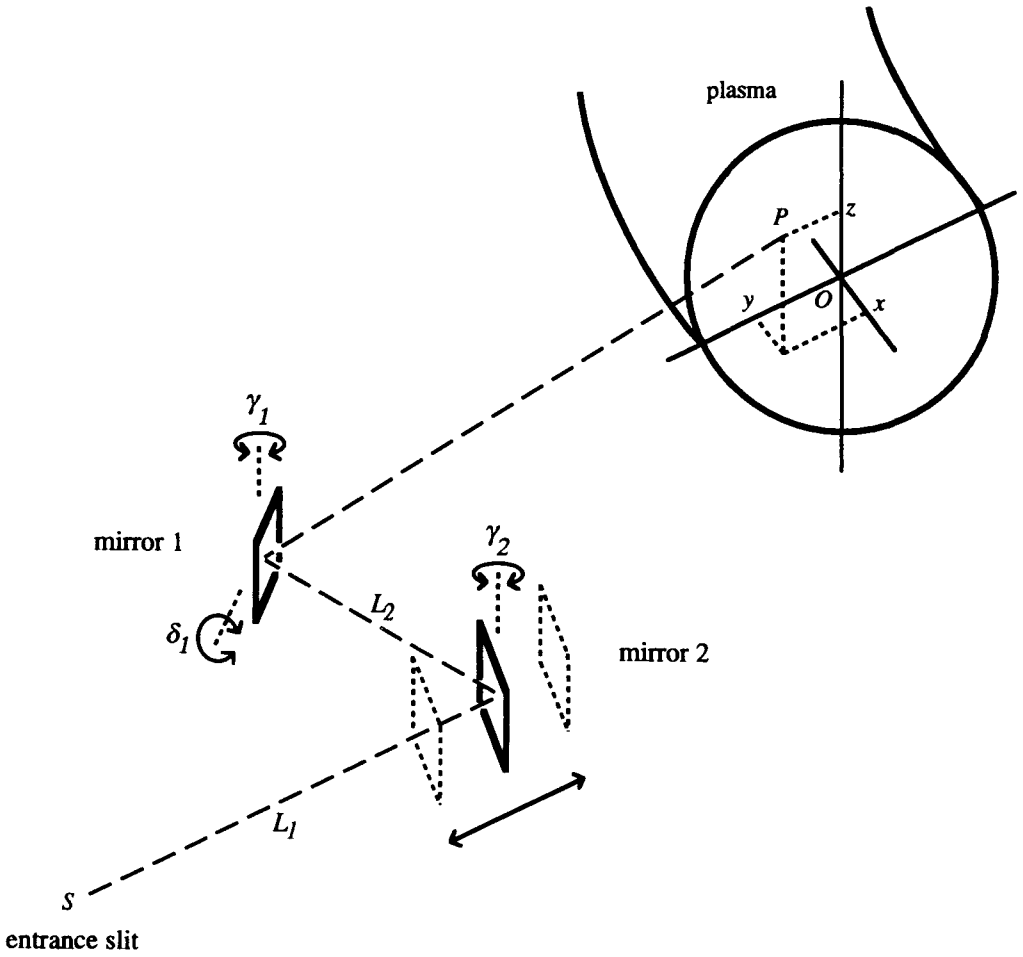

Figure A2.1 - Schematic view of the scanning mirror system. We use a Carthesian co-ordinate system in the plasma region coverred.

Vertical scan (z-direction)

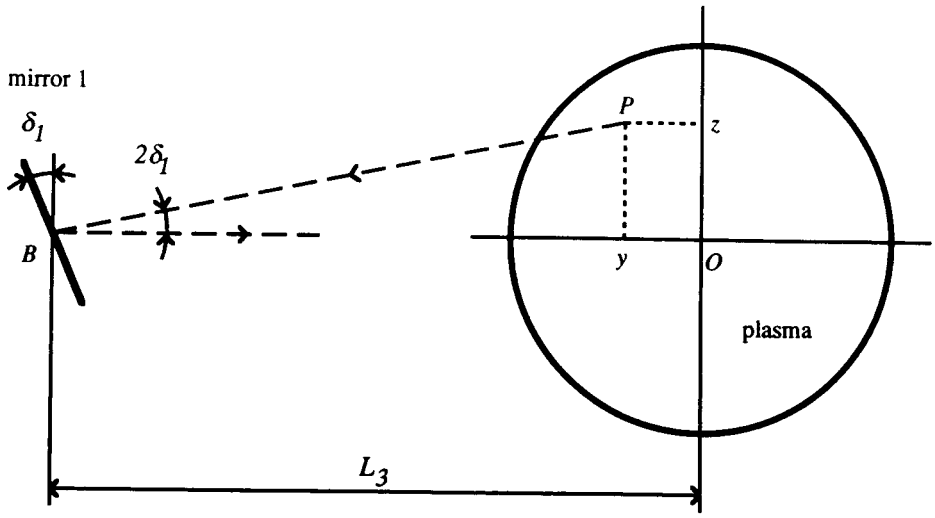

Figure A2.2 - Side view of mirror 1. The tilting angle δ_1 determines the z-co-ordinate of the source point P in the plasma. The circle indicates a poloidal cross-section of the plasma.

Consider figure A2.2. The vertical scan is performed by tilting mirror 1 around a horizontal axis. The tilting angle δ_1 determines the z-co-ordinate of the source point:

$$z = (L_3 - y) \tan(2\delta_1) \approx 2\delta_1 (L_3 - y) \qquad \text{(A2.1)}$$

or

$$\delta_1 \approx \frac{z}{2 (L_3 - y)} . \qquad \text{(A2.2)}$$

Depth scan (*y*-direction)

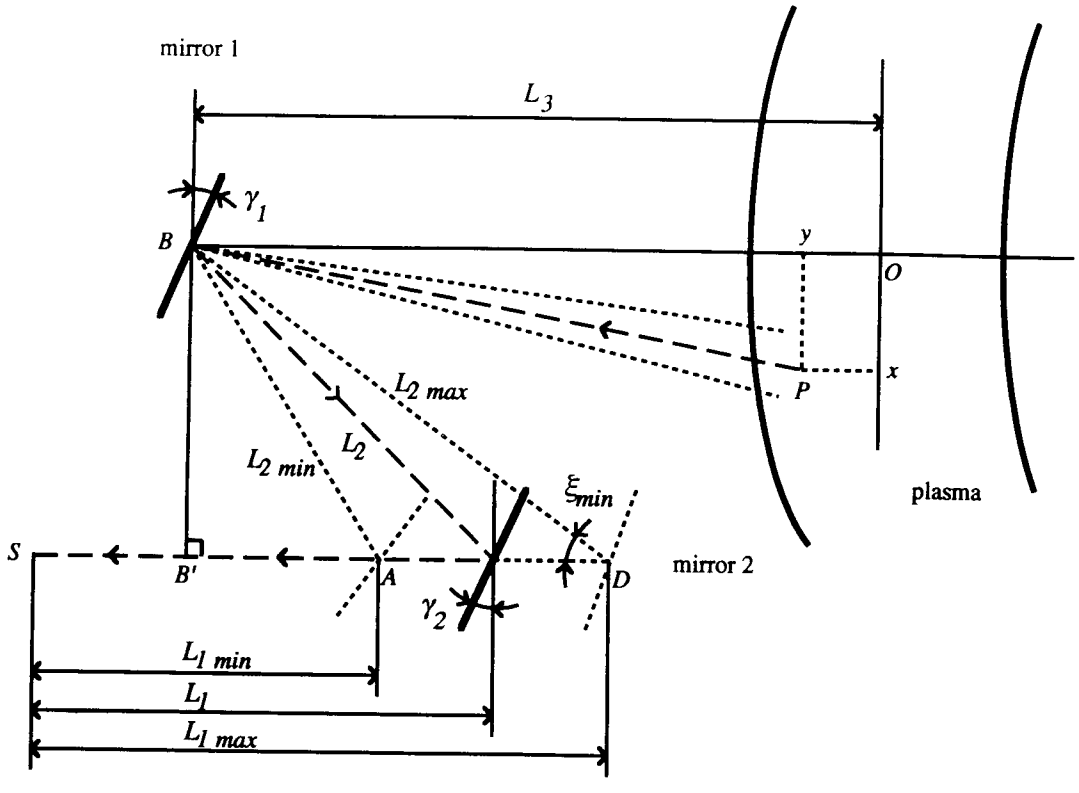

Figure A2.3 - Top view of the scanning mirror system. S is the entrance slit. The arrowed lines indicate the path of light. Turning mirror 1 around its vertical axis gives a scan in horizontal direction (x-co-ordinate). A depth scan (y-co-ordinate) can be accomplished by changing the distance L_2 between the two mirrors. This distance can be changed between $L_{2\ min}$ and $L_{2\ max}$ by moving mirror 2 between its end positions A and D. The small-dashed lines give the paths of light in case of those end positions. Optical contact between both mirrors is provided by turning mirror 2 around its vertical axis.

The system of two hollow mirrors acts the same as a system of two convex lenses, so a depth scan can be accomplished by changing the distance L_2 between the two mirrors. This distance can be changed between $L_{2\ min}$ and $L_{2\ max}$ by moving mirror 2 between its end positions *A* and *D* (figure A2.3). The used mirrors have focal lengths f_1 = 4 m and f_2 = 2 m.

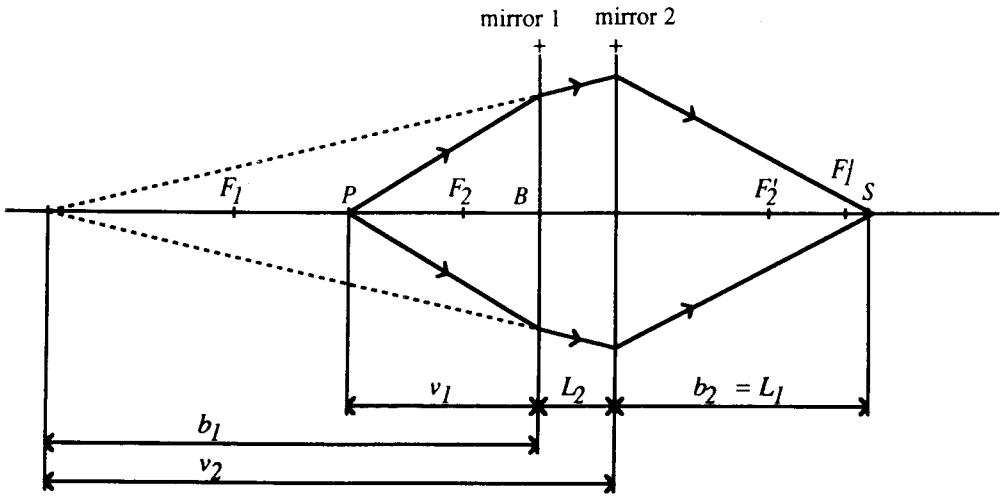

Figure A2.4 - The lens analogue of the two mirror system, projected on a straight line. Mirror 1 forms a virtual image of the source point P in the plasma. This image is the object of mirror 2, which on turn focuses its image on the slit S. The focal points F_1, F_2, F_1' and F_2'; the object distances v_1 and v_2, and the image distances b_1 and b_2 are indicated.

Figure A2.4 gives the lens analogue of the two mirror system, projected on a straight line. With the help of figure A2.3 and A2.4 we can derive a relation between L_1 and the position of the source point P in the plasma. All symbols are explained in the figures.
The object of mirror 1 is the source point in the plasma:

$$v_1 = PB = \sqrt{(L_3 - y)^2 + x^2 + z^2} \; . \qquad \text{(A2.3)}$$

Its virtual image is the object of mirror 2:

$$v_2 = b_1 + L_2 \; . \qquad \text{(A2.4)}$$

On his turn, mirror 2 focuses its real image on the slit, so

$$b_2 = L_1 \; . \qquad \text{(A2.5)}$$

For each mirror we can apply the well-known "lens" formula:

$$b_1 = \frac{v_1 f_1}{f_1 - v_1} \tag{A2.6}$$

for the mirror 1, and

$$b_2 = \frac{v_2 f_2}{v_2 - f_2} \tag{A2.7}$$

for mirror 2, respectively. All distances are taken positive. The lens formulas have been adapted to the virtual or real image of the corresponding mirror. Using (A2.3) and (A2.6), we find an expression for the image distance of mirror 1:

$$b_1 = \frac{f_1 \sqrt{(L_3 - y)^2 + x^2 + z^2}}{f_1 - \sqrt{(L_3 - y)^2 + x^2 + z^2}} . \tag{A2.8}$$

From (A2.4), (A2.5) and (A2.7) we find

$$b_2 = L_1 = \frac{(b_1 + L_2) f_2}{b_1 + L_2 - f_2} \tag{A2.9}$$

$$\Rightarrow \quad L_2 = \frac{b_1 f_2 + L_1 (f_2 - b_1)}{(L_1 - f_2)} . \tag{A2.10}$$

Using the Pythagorean theorem, it follows from figure A2.3 that

$$(L_2)^2 = (BB')^2 + (L_1 - SB')^2 \tag{A2.11}$$

Combining the latter two formulas, we can derive the following equation for L_1:

$$(BB')^2 + (L_1 - SB')^2 = \left(\frac{b_1 f_2 + L_1 (f_2 - b_1)}{(L_1 - f_2)} \right)^2 , \tag{A2.12}$$

where b_1 is given by (A2.8). This forth order polynomial equation can only be resolved numerically. Notice that for determining BB' and SB', there is no need to know the exact position of B'. It is enough to know the distances AB ($= L_{2\,min}$), BD ($= L_{2\,max}$) and AD, which can simply be measured:

$$BB' = BD \sin \xi_{min} \tag{A2.13}$$

and

$$\begin{aligned} SB' &= L_{1\,min} + AD - B'D \\ &= L_{1\,min} + AD - BD \cos \xi_{min} , \end{aligned} \tag{A2.14}$$

where

$$\cos \xi_{min} = \left(\frac{AD^2 + BD^2 - AB^2}{2\,AD\,BD} \right) \qquad \text{(A2.15)}$$

follows from the cosine rule.

Both mirrors have to keep optical contact when shifting mirror 2. This determines the turning angle γ_2 of mirror 2:

$$\gamma_2 = \tfrac{1}{2} \arctan \left(\frac{BB'}{L_1 - SB'} \right) . \qquad \text{(A2.16)}$$

As mentioned before, we can resolve L_1, that is the linear position of mirror 2, as a function of y, by substituting (A2.8) in (A2.12) and resolve the latter equation numerically.

Horizontal viewing line (x-direction)

Again consider figure A2.3. The horizontal viewing line can be adjusted by turning mirror 1 around its vertical axis. We can derive the following relation between turning angle γ_1 and the x-co-ordinate in the plasma:

$$\gamma_1 = \gamma_2 + \tfrac{1}{2} \arctan \left(\frac{x}{L_3} \right) . \qquad \text{(A2.17)}$$

In practice L_1 and L_3 are not parallel to the y-axis as was taken for simplicity. This can simply be solved by fixing the x-co-ordinate to a position x_0 corresponding to a viewing line lying in a poloidal plane. This position minimises coma.

Appendix 3

Vacuum control system

The vacuum system of the NIS as described in paragraph 3.2, is controlled by an electromechanical "dedicated computer". This is because of its reliability in the semi-conductor unfriendly environment. All logic components are built with relays. This appendix gives the electrical schemes, completed by a brief explanation. In the schemes, the different types of contacts are coded by colour. The meaning of each colour is explained in figure A3.1. This figure also gives a list of al pumps, valves and cooling systems used, and a list of all signalling lamps, sorted by colour. Further, a list of all relays and their functions is given. A survey of all logic rules the control system takes care of, is given in figure A3.2.

Legend

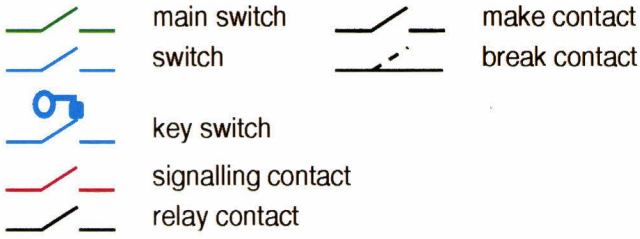

Pumps

DP I	diffusion pump I
VP I	rotary pump I
VP II	rotary pump II

Valves

HVV	high vacuum valve
BV	backing valve
RV I	roughing valve I
RV II	roughing valve II
IV	insulation valve (between tank compartments)
AR I	air release valve I
AR II	air release valve II
AR III	auto air release on VP I
AR IV	auto air release on VP II
V I	valve I
V II	valve II

Cooling systems

DP I & HVV	cooling diffusion pump I and high vacuum valve
CB I	cooling Chevron baffle I

Indicating and signalling lamps

green	all valves all pumps
white	all cooling systems motor valve IV on
red	cooling DP I and HVV low cooling CB I low temperature DP I too high backing pressure DP I too high (can be overruled by S3) mirror (no light at detector) alarm (DP I fails after first been on)
flashing neon	DP I on and BV closed
no lamp	2 phase power failure DP I 3 phase power failure VP I and VP II auto thermal fuse VP I and VP II
siren	alarm (DP I fails after first been on)

Relays

1.1 (3phase)	DP I
1.2	DP I
2.1 (3 phase)	VP I
2.2	VP I
2.3	3 phase power control VP I
3.1 (3 phase)	VP II
3.2	VP II
3.3	3 phase power control VP II
4	HVV
5	BV
6a + 6b	RV I
7a + 7b	RV II
8a + 8b	IV
9	AR I
10	AR II
11a + 11b	V I
12.1	V II
12.2	V II
13	cooling DP I and HVV low
14	cooling CB I low
15	temperature DP I too high
16	backing pressure DP I too high
17	siren control
18	motor IV
19	motor IV
20	reversal relay for temp. DP I
21	3 phase power control (R)
22	3 phase power control (S)
23	3 phase power control (T)

Other Abbreviations (relays lay–out)

Temp	temperature
Back	backing pressure
Alrm	alarm
Mir	mirror
Cool.	cooling
Sign.	signalling contact

Figure A3.1 – Legend, list of pumps, valves, cooling systems, indicating and signalling lamps, relays and other abbreviations

- Pump DP I (H1/D1) can only be switched on if :
  - Cooling DP I and HVV on
  - Cooling CB I on
  - 2 phase power DP I present
  - VP I on
  - Signalizings OK (cooling flow DP I and HVV not low, cooling flow CB I not low; temperature DP I not too high; backing pressure not too high; reset D17)

- Pump VP I (H2/D2) can be switched on if 3 phase power VP I present; auto thermal fuse

- Pump VP II (H3/D3) can be switched on if 3 phase power VP II present; auto thermal fuse

- Valve HVV (D4/D5) can only be opened if : BV open, RV I, AR I, (V I or V II), (IV or (RV II and AR II)) closed, and DP I on

- Valve BV (D6/D7) can only be opened if : RV I closed, and VP I on

- Valve RV I (D8/D9) can only be opened if : HVV, IV, AR I, BV , (V I or V II) closed, VP I on, and backing pressure not too high

- Valve RV II (D10/D11) can only be opened if : IV, AR II closed, and VP II on

- Valve IV (D12/S6) can only be opened if : RV I, RV II, AR I, AR II, (V I or V II) closed

- Valve AR I (S4 key) can only be opened if : HVV, RV I, IV, (V I or V II) closed

- Valve AR II (S5 key) can only be opened if : RV II, IV closed

- Valves AR III and AR IV are automatic air release valves on VP I and VP II

- Valve V I (D14/D15) can only be opened if : V II closed, and VP II on

- Manual valve V II is signalized only, an can be opened any time

- Siren (reset: D16 or H1) turns on when diffusionpump DP I, after first been on, fails

- Flashing neon light when DP I on and BV closed (may not stay for longer then app. half an hour; timer in option)

- Backing pressure control can be overruled by key switch (S3 key)

Figure A3.2 – List of all logic rules the control system takes care of

A3.1 Description of the electrical schemes

The electrical schemes are given in the figures A3.3 up to A3.8 inclusive. The electrical structure is the same for all valves and pumps. Each valve is switched indirectly by a relay, and has two separated buttons for opening and closing. A valve can only be opened when the conditions programmed by the tree of contacts serial to the relay, are met. Parallel contacts form a logic OR, serial contacts a logic AND. The pumps only have a switch-on button. They are switched off by the main switches H1, H2 and H3 respectively. We will now discuss some points of special interest for each scheme. To provide for fast searching, the figure numbers of the corresponding electrical schemes are given between brackets in the headings.

DP I, VP I, VP II and siren (fig. A3.3)

The pumps are switch by the 3-phase power relays 1.1, 2.1 and 3.1. The oil diffusion pump DP I uses only two phases. Its zero line is doubled concerning the high current. The power relays are coupled back by the relays 1.2, 2.2 and 3.2 respectively. Notice that relay 1.2 is directly connected to the power connections of the diffusion pump, instead of being switched by a relay contact like the other two relays (see also figure A3.9). The currents of the two rough vacuum pumps are controlled by automatic thermal fuses, which also provide a 3-phase power control: when one phase drops, the current of the other two increases above the limit. The relays 2.3 and 3.3 take care of the situation when all three phases fail. The 3-phase control unit existing of relays 21, 22 and 23 is used for DP I.
The circuit parallel to relay 1.1 gives a flashing neon light when valve BV is closed while diffusion pump DP I is switched on. This situation may not stay for longer then approximately half an hour, because DP I cannot release its pumped gas.
A fail save alarm circuit is constructed around relay 17. The siren and alarm light are switched on when DP I fails, after first have been on. In this way all signallings are covered, as they are all conditions to enable the diffusion pump. D16 is the alarm reset button.

HVV, BV, RV I and RV II (fig. A3.4)

The air pressure controlled high vacuum valve HVV has a signalling contact. The double use of contact 5b is only to save an extra relay.

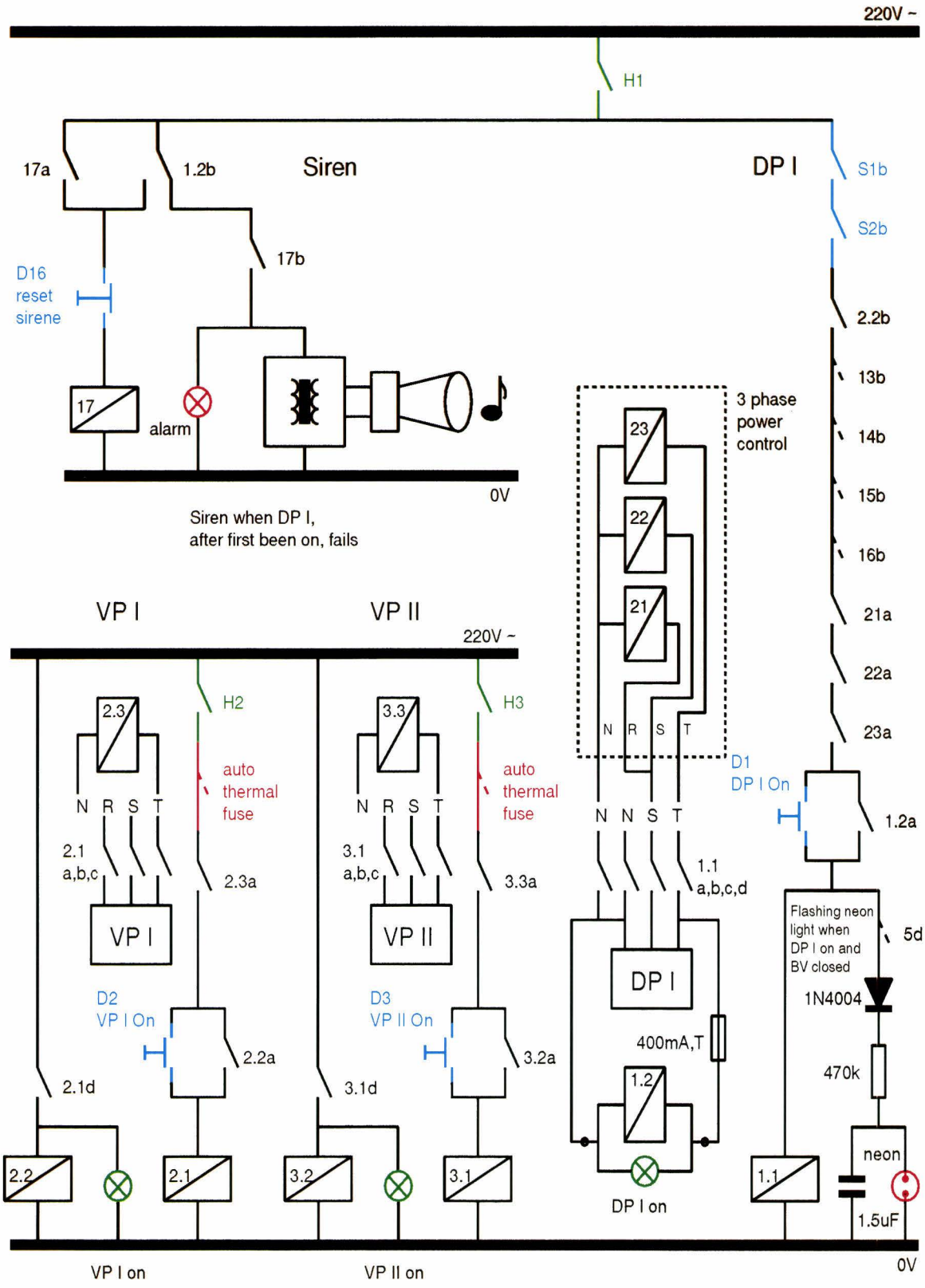

Figure A3.3 – Electrical schemes for pumps (DP I, VP I and VP II) and siren

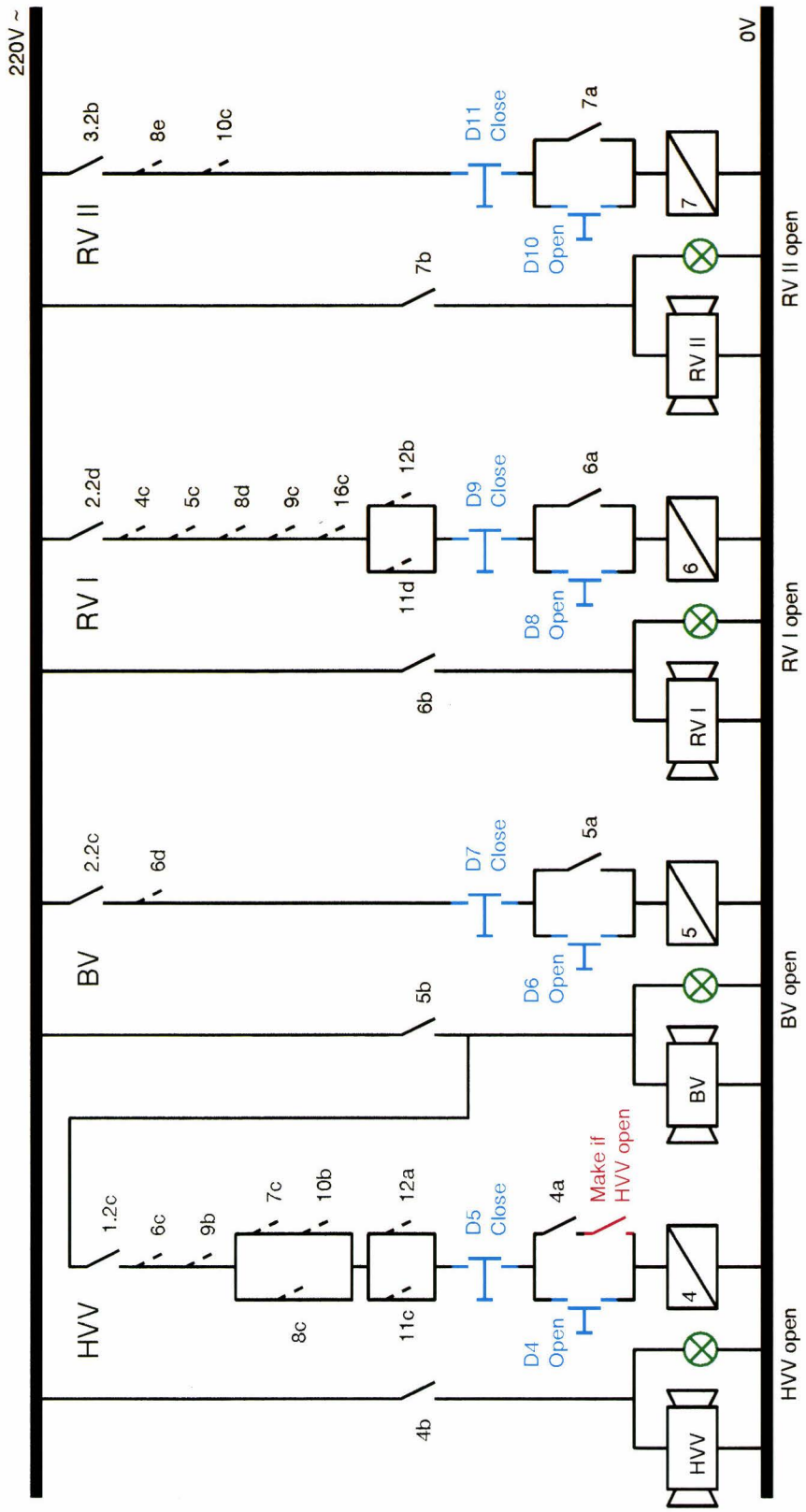

Figure A3.4 – Electrical schemes for the valves HVV, BV, RV I and RV II

IV (fig. A3.5)

The insulation valve IV between the two tank compartments is driven by a dc current motor, and has its own 24V circuit. When all conditions programmed by the tree of contacts 6e - 12c are met, relay 8 can be powered by closing manual switch S6. Contact 8a then closes and the valve can be opened as far as necessary by holding button D12. The green lamp lights as soon as the valve is not fully closed. The white lamp lights as long as the motor is running. When leaving the button, the valve keeps its current position. When relay 8 drops, either by opening S6 or automatically when the conditions are no longer met, contact 8b is closed, also closing the valve. The ending-micro switches prevent damage to motor and valve. Because of the large motor current, the contacts of relays 18 and 19 are used parallel.

AR I, AR II, V I, V II (fig. A3.6)

The air release valves AR I and AR II are controlled by key switches. The air release valves AR III and AR IV (not in the schemes) are opened automatically when the rough vacuum pumps are switched off. Valve V II is a signalled manual valve.

Cooling systems (fig. A3.7) and Signalling (fig. A3.8)

Both cooling systems are controlled by electromechanical valves. Low cooling flows are signalled, as is a too high temperature or backing pressure of the diffusion pump. When necessary, e.g. during the starting procedure of the vacuum system, the backing pressure control can be switched off by key switch S3. These four signallings have a common reset button D17, working independently of the alarm reset. The position of the mirror directly behind the entrance slit is also signalled. Relay 20 is only used to reverse the contact of the temperature measurement of the diffusion pump.

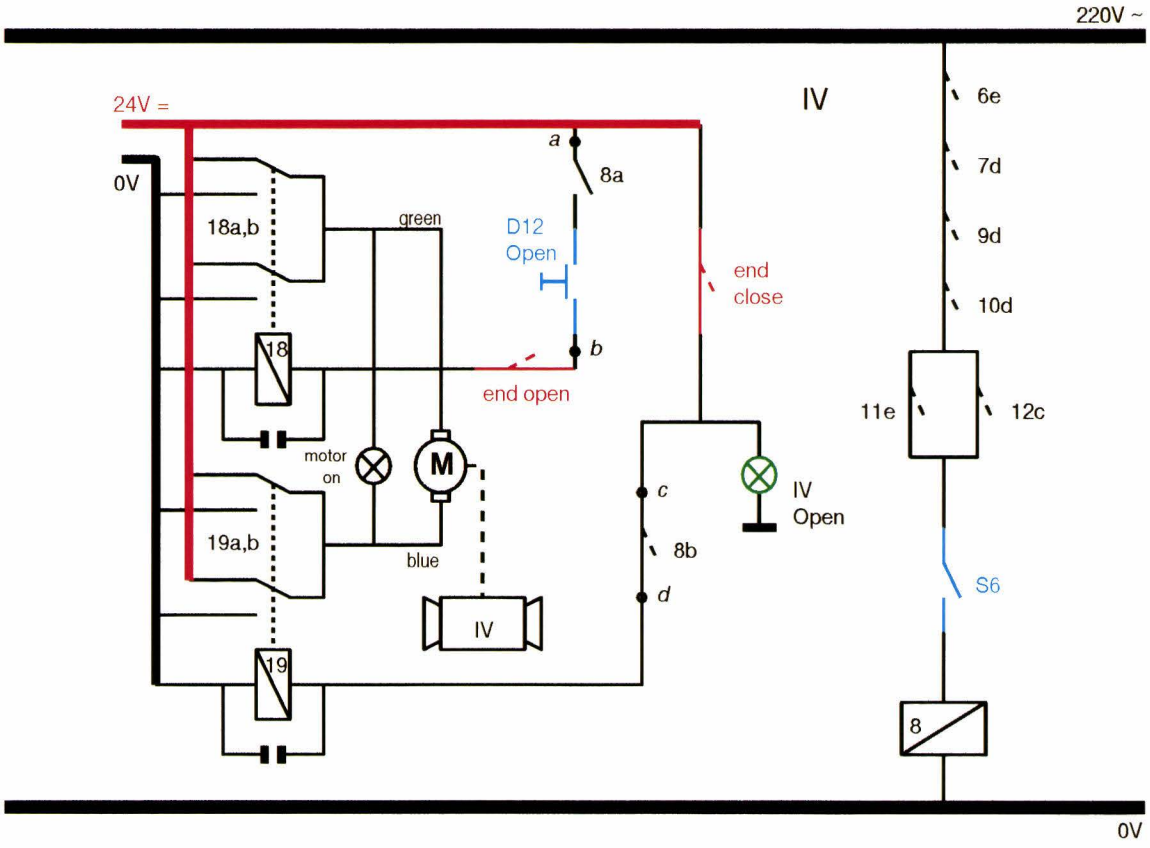

Figure A3.5 – Electrical scheme for valve IV

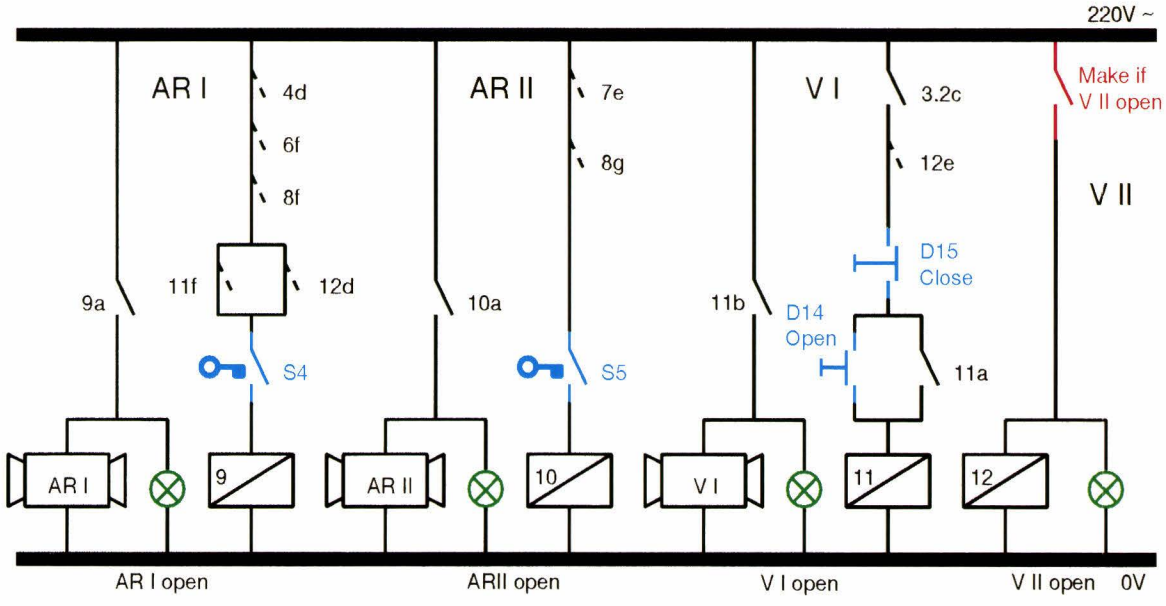

Figure A3.6 – Electrical schemes for the valves AR I, AR II, V I and V II

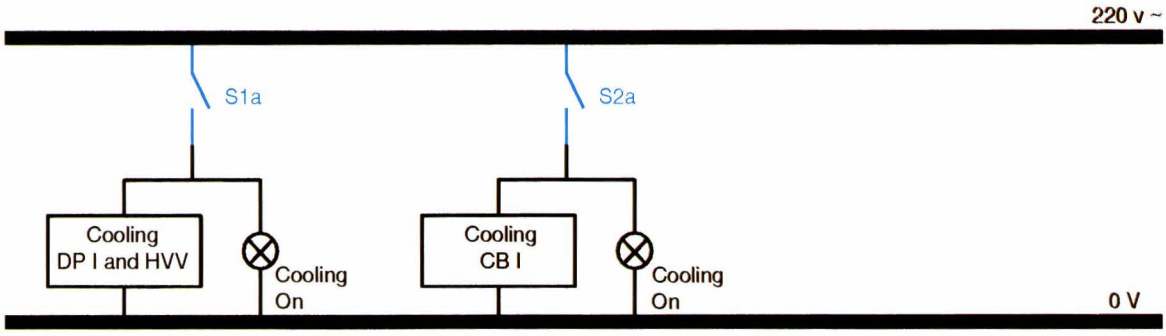

Figure A3.7 – Electrical schemes for the cooling systems

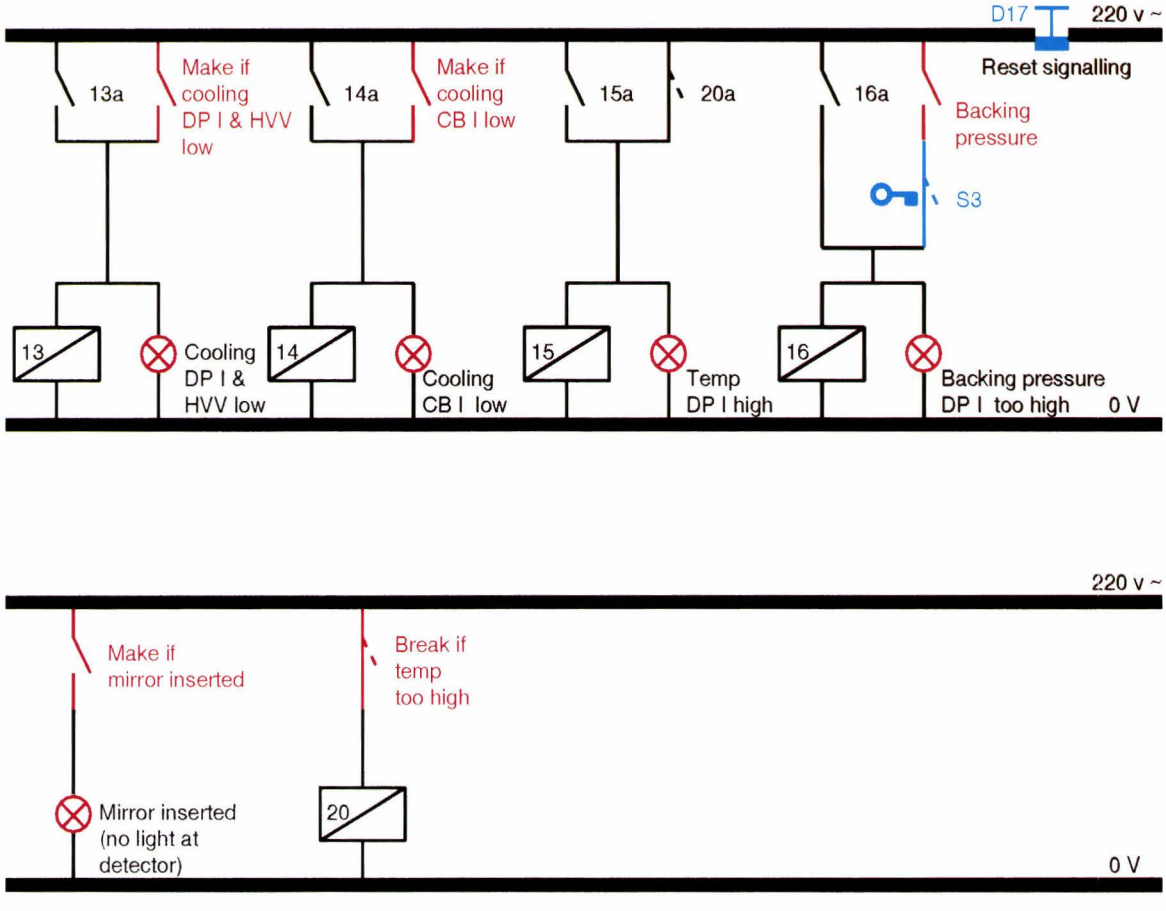

Figure A3.8 – Electrical schemes for the signalling systems

A3.2 Connector lay-outs

Figure A3.9 gives the lay-out of the relay mounting plates. Most relays are mounted on these two plates. The numbers and abbreviations refer to the electrical schemes and are explained in figure A3.1. Both 24 V relays 18 and 19 from figure A3.5 have their own plate (figure A3.10). The remaining relays are mounted near to the pumps.

The upper row of connector strips of plate one and all three rows of plate two are used for the relay coils and contacts. Each relay has its coil and (part of) its contacts connected to these connector strips as indicated in figure A3.9. This gives us a set of "ready to use" relays. The three remaining rows of connector strips on plate one are used for the in- and output connections with the switches and buttons, the valves and their parallel switched lamps, the signalling contacts, the 24 V-plate, et cetera. Again in the figure is indicated which button, valve, etc. is connected to which connector position. Button number D13 is not used. The colour of each connector strip contact indicates the corresponding wire colour (not to be confused with the colours used in the electrical schemes!). The meanings of the colours are explained in figure A3.9.

So far all connections can be seen as "hardware" and do *not* have to be changed when one wants to change the logic rules. Only the "programming" connections (red wires) have to be changed. There is no need for measuring or following wires, because they can all be identified by their beginning and end connections, which can be found easily in the lay-outs. This, and the uniform electrical structure makes changing of the logic rules quite easy.

Finally, figure A3.11 gives the lay-out of the "220V-connector", built of two rows of connector strips. It connects the vacuum control system with the NIS.

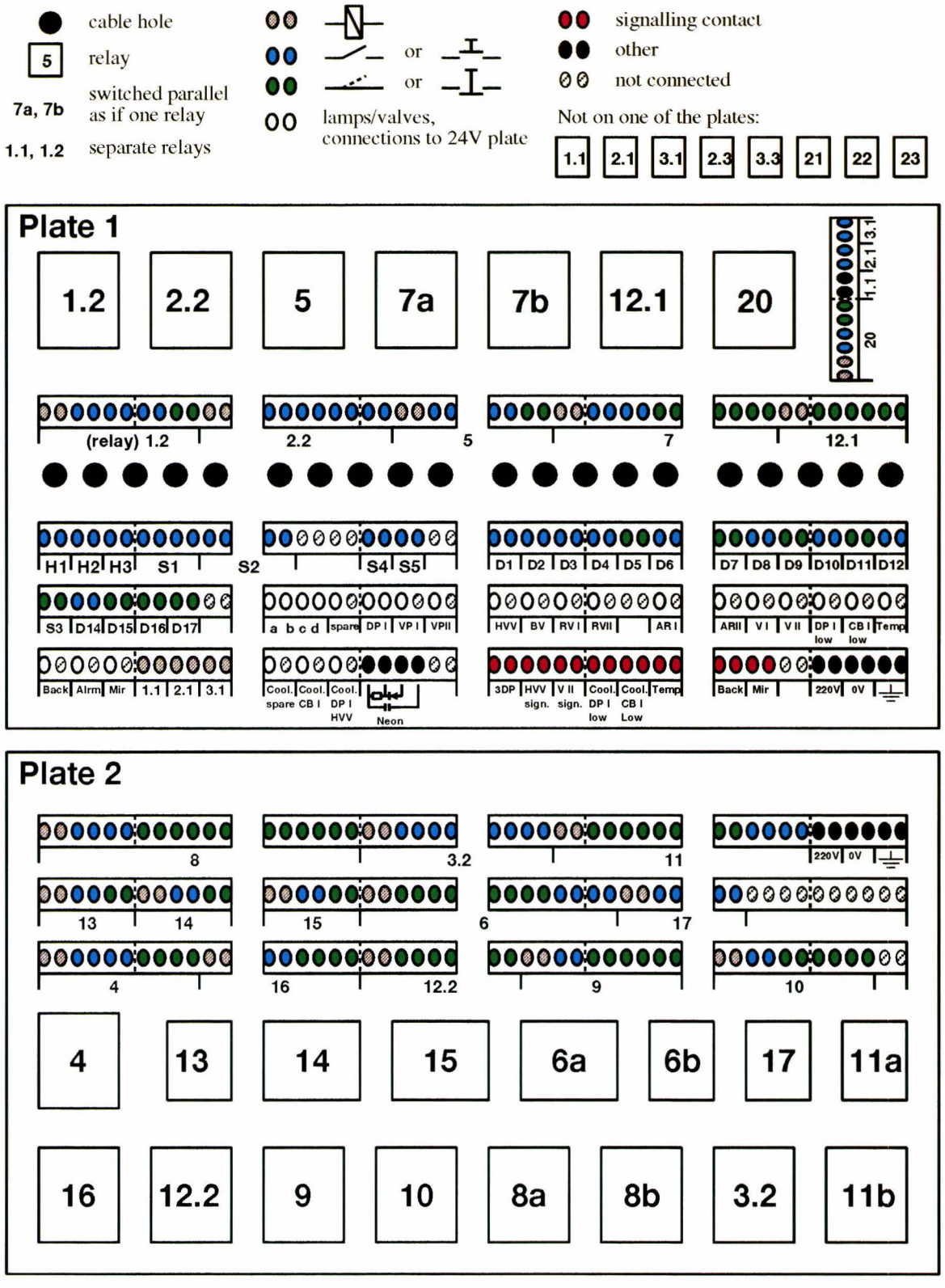

Figure A3.9 – Lay-out of the relay mounting plates. The numbers and abbreviations refer to the electrical schemes (see figure A3.1). The colour of the connector strip contacts indicate the corresponding wire colour. The meanings of the colours are: blue for all make contacts (relay contacts, switches and buttons); green for all break contacts; grey for the connections to the relay coils; red for the signalling contacts; white for the connections to the valves (including those for the cooling systems) and their parallel switched lamps, and for the connections to the 24V plate. The latter connections are marked a – d, referring to the points indicated in figure A3.5 and A3.10. Finally, black is used for the remaining wire colours: brown (220 V lines) and black (0 V lines). The black connections in the vertical mounted connector strip refer to the different back coupling of relay 1.1: the connections marked 2.1 and 3.1 are open contacts, while 1.1 gives a 220 V signal (see figure A3.3). Button number D13 is not used.

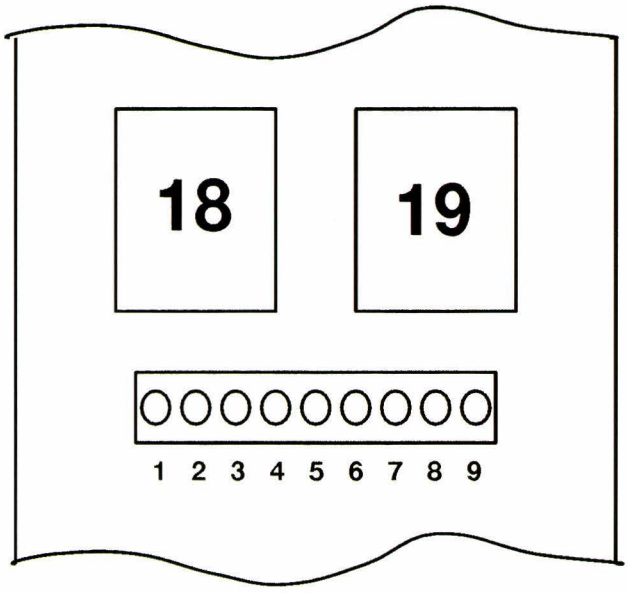

18 = relays

Connector:

1 end open
2 end open, b
3 end close, lamp IV, c
4 d
5 0 V, lamp IV
6 motor, lamp motor
7 motor, lamp motor
8 end close, a
9 24 V

Figure A3.10 – Lay–out of the connector at the 24 V plate (see figure A3.5). "End open" and "end close" refer to the microswitches. The letters a – d refer to the points indicated in figure A3.5.

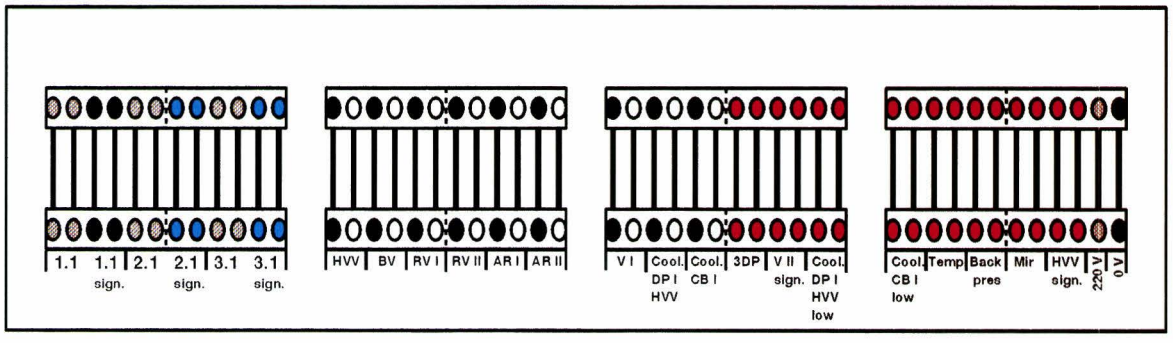

Figure A3.11 – Lay–out of the connector to the NIS. This 48–pin "220 V power–connector" is built of two rows of connector strips. The numbers and abbreviations refer to the electrical schemes (see figure A3.1). The colours are explained in figure A3.9.

Dankwoord

Rijnhuizen is ongetwijfeld iets unieks. Komt het door het kasteel, het park en het pluimvee (ja, ook die ~~drie~~ ene grote)? Of door de sportdag, het volleybaltoornooi en het cabaret? Waarschijnlijk komt het vooral door het bonte gezelschap dat hier tot diep in de avond nog "plasma's zit te schieten". Zonder iemand tekort te doen, wil ik enkele collega's toch in het bijzonder noemen.

Om te beginnen mijn begeleider Frans Meijer ("Beneden in de kelder heb ik geloof ik nog ergens een klepje liggen.."), en mijn dagelijkse collega's Janco "Zeker weten" van Rijswijk en Peter van den Os (expert op het gebied van motortjes, connectoren en het beheer van onze gezamenlijke voorraad kladpapier). Samen hebben we het gevecht met de NIS aangedurft. Met als belangrijkste wapens: een hoop denkwerk, ontelbare kabelbindertjes (ongelofelijk wat je daar allemaal niet mee kunt doen, hè Frans!), 44 gloeilampjes, dozen vol zekeringen en een onbegrensd enthousiasme. Maar het resultaat mag er zijn: een geheel geautomatiseerde, veelzijdige en vooral gigantische (wie kan er nog meer zeggen dat zijn diagnostiek groter is dan de tokamak zelf?) diagnostiek. Wie hebben er nog meer hun bijdrage geleverd aan dit mega-project? In willekeurige volgorde, Paul Smeets (is er een verband tussen de NIS en de aanleg van een aardfout-detector?), Paul Haarbos (zijn naam is vereeuwigd op het beton van de NIS), Cor Tito (voor zijn vacuum-adviezen (en zijn gereedschap...)), de dames van het secretariaat, in het bijzonder Laura (het overgrote deel van dit verslag kwam op haar "Mac" tot stand), Cor Dorjee (mijn steun en toeverlaat in de avonduurtjes), Michel en Kees van het magazijn ("kom je nou alweer kabel halen?"), en de voltallige crew van de werkplaats (voor de vele kleine en grotere klusjes). Verder mogen ook niet onvermeld blijven: Daan Schram (voor zijn nuttige opmerkingen met betrekking tot dit verslag), Niek Lopes Cardoso (voor het overnemen van het afstudeerdocentschap), Tony "Fusion Expo" Donné, Bart, Marc en Frieke (samen hebben we Nederland warm gemaakt voor kernfusie, hoop ik), mijn kamergenoten (voor zover nog niet genoemd) Lei, Jos, Frank, en Jesùs (voor de altijd gezellige sfeer), en alle andere mede-FOM-ers.